

## Article

# Hybrid Renewable Energy System for Terminos Lagoon, Campeche, Mexico

César Sánchez-Rucobo y Huerdo <sup>1</sup>, Ma. Eugenia Allende-Arandía <sup>2,\*</sup>, Bernardo Figueroa-Espinoza <sup>2</sup>, Estefanía García-Caballero <sup>1</sup>, Adolfo Contreras-Ruiz Esparza <sup>3</sup> and Christian M. Appendini <sup>2,\*</sup>

<sup>1</sup> Programa de Maestría y Doctorado en Ingeniería, Universidad Nacional Autónoma de México, Ciudad de México 04510, Mexico

<sup>2</sup> Laboratorio de Ingeniería y Procesos Costeros, Instituto de Ingeniería, Universidad Nacional Autónoma de México, Puerto de Abrigo s/n, Sisal 97356, Mexico

<sup>3</sup> Energy and Climate Branch United Nations Environment Programme, 75015 Paris, France

\* Correspondence: mallendea@iingen.unam.mx (M.E.A.-A.); cappendini@iingen.unam.mx (C.M.A.); Tel.: +52-988-931-1000 (M.E.A.-A.)

**Abstract:** The implementation of renewable energies represents a crucial step in meeting the sustainable development goal of the United Nations for affordable and clean energy. The Terminos Lagoon region in Campeche, the largest coastal lagoon in Mexico, offers potential for renewable energy sources such as wind, photovoltaic, and current energy. This study presents a renewable energy potential assessment for the main city at Terminos Lagoon, Ciudad del Carmen, which has the largest oil activity in Mexico and high electricity consumption. The outputs of high-resolution numerical models were analyzed to evaluate wind and photovoltaic resources and currents. A hybrid system consisting of 24 wind turbines, 5516 photovoltaic panels, and 32 hydrokinetic turbines could generate 521.33 GWh, which is 39.63% of the state's energy demand and exceeds the energy consumption of Ciudad del Carmen by 10.24%. Wind and photovoltaic energy are the most significant contributors (517.15 GWh and 3.77 GWh, respectively), while hydrokinetic energy contribution is marginal (0.407 GWh) and requires further research and development. The results suggest that the region has the potential for clean and renewable energy technologies to reduce greenhouse gas emissions and contribute to the energy transition.

**Keywords:** hybrid system; terminos lagoon; renewable energy; wind turbines; photovoltaic panels; hydrokinetic turbines



**Citation:** Sánchez-Rucobo y Huerdo, C.; Allende-Arandía, M.E.; Figueroa-Espinoza, B.; García-Caballero, E.; Esparza, A.C.-R.; Appendini, C.M. Hybrid Renewable Energy System for Terminos Lagoon, Campeche, Mexico. *Energies* **2023**, *16*, 3972. <https://doi.org/10.3390/en16103972>

Academic Editor: Branislav Hredzak

Received: 4 April 2023

Revised: 27 April 2023

Accepted: 28 April 2023

Published: 9 May 2023



**Copyright:** © 2023 by the authors. Licensee MDPI, Basel, Switzerland. This article is an open access article distributed under the terms and conditions of the Creative Commons Attribution (CC BY) license (<https://creativecommons.org/licenses/by/4.0/>).

## 1. Introduction

The use of fossil fuels has contributed to global warming due to the emission of greenhouse gasses [1]. In recent years, alternative energy sources have been explored to mitigate the environmental impact and to meet the growing energy demand due to anthropogenic development [2]. As a result, harnessing renewable energies has become a focus of research. These energies are regenerated naturally in a short time scale and include solar, wind, hydroelectric, biomass, geothermal, and tidal power. Renewable energies have gradually gained importance worldwide to replace the traditional energy system, since conventional energy generation contributes 80% of greenhouse gas emissions [3]. Many renewable energy technologies have matured and evolved in recent decades, increasing their reliability and profitability for various applications worldwide [4]. Policies that favor renewable energies over fossil fuels have contributed to their growth, as well as the climatic conditions and other factors that play a key role in global electricity production [5]. More recently, the United Nations Sustainable Development Goal for affordable and clean energy exerts a significant influence in promoting clean and renewable energies.

Due to its geographical location and territorial extension, Mexico has great potential in renewable energy resources [4,6]; however, it has not been sufficiently exploited. In

particular, the Gulf of Mexico (GoM) coastal region is strongly influenced by trade winds and sea breezes [7,8], where several studies underscore the wind energy potential in the region [9,10]. Ref. [9] highlights the state of Campeche as a region with a significant wind potential, as it presents strong winds with an average of  $7.47 \text{ ms}^{-1}$ , which during winter and spring have intensities just below those of Tamaulipas and the north and south of Veracruz; states with the largest wind resource in the GoM region. Studies by [6,11] indicate that Mexico has excellent solar potential throughout the year. Ref. [12] confirms that the state of Campeche has adequate irradiation for thermal and photovoltaic generation, exceeding  $4 \text{ kWh m}^{-2} \text{ day}^{-1}$ . While Mexico still lags behind several countries in installed solar capacity and growth, it has a significant advantage in solar radiation levels and a largely untapped market for solar energy development. Ref. [13] conducted a comparative analysis of the photovoltaic sector in Mexico and Germany, revealing that Mexico has significant potential to become a major player in the use of renewable energy. The authors noted that Mexico has substantial photovoltaic solar potential, and with appropriate policies and incentives, could position itself as an important producer of photovoltaic energy, akin to Germany, which has emerged among the top world leaders in photovoltaic technology generation and development. Refs. [9,14] indicate that Mexico's wind and photovoltaic potential is favorable, and these energy sources complement each other for energy generation. Regarding tidal and ocean currents power, there are studies reporting the energy potential for areas in the Gulf of California and the Yucatan Current area, including the Cozumel Island Channel [15–17]. However, information on coastal lagoons is limited, despite the potential for narrow inlets to create high-speed currents suitable for power generation [18].

Considering the mismatch between energy demand and renewable energy production, hybrid renewable energy systems appear as an alternative that can improve efficiency and reliability, minimizing storage capacity [19]. Additionally, hybrid renewable energy systems provide an opportunity for developing countries to develop reliable and cost-effective off-grid power for communities [20]. As such, we present a study to evaluate the renewable energy potential to propose a hybrid renewable energy system for Ciudad del Carmen, Mexico, one of the most important cities in the state of Campeche and the country's largest oil city. Ciudad del Carmen is located over the barrier island of the Terminos Lagoon (TL) in the southeast of Mexico. The Federal Electricity Commission's report shows that in 2018, the state of Campeche consumed an average of 1315.61 GWh with 103.43 GWh consumed by May 2019. Meanwhile, Ciudad del Carmen consumed 472.9 GWh in 2018 and 37.1 GWh by May of the same year.

This study analyzes and characterizes the TL region's natural physical processes and power resources to evaluate its energy potential. The study uses the Weather Research and Forecasting Model (WRF) data to characterize wind, determine wind potential, and assess the incident solar radiation and photovoltaic potential. Additionally, the oceanic model MARS3D of IFREMER, France, and tidal predictions from the MarV1.0 tool of the Scientific Research and Higher Education Center of Ensenada (CICESE) are used to characterize tidal currents and calculate energy potential.

## 2. Data and Methods

### 2.1. Study Area

The study area encompasses the region of the TL, located at  $18^{\circ}01'54''$ – $19^{\circ}13'33''$  North and  $92^{\circ}32'33''$ – $90^{\circ}59'15''$  West, in the coastal zone of the state of Campeche, Mexico (Figure 1). TL has borders with the Yucatan Peninsula at the east, the coastal floodplain of Tabasco at the west, and the GoM at the north. It is part of a lagoon system formed by nine satellite lagoons: Pom, Atasta; El Corte, Puerto Rico; Los Negros at the southwest, connected to the TL through the Atasta mouth; Sabancuy estuary to the northeast; Panlao lagoon in the southeast; and Balchacah and the East lagoons at the south. TL is Mexico's largest coastal lagoon, stretching 75 km along the coast and reaching a maximum width of 26.3 km. It forms part of the country's largest coastal ecosystem [21,22]. TL is separated from the GoM by two limestone-sand Holocene barrier islands [23,24]. Firstly, Isla del

Carmen has 38 km in length and 2.5 km of width. Secondly, Isla Aguada has 40 km in length and 900 m in width. TL connects to the GoM through two natural inlets: the Puerto Real (PtR) northeast and the Ciudad del Carmen (CdC) northwest. PtR inlet has a width of 3.2 km and an average depth of 5 m, located between Isla Aguada and Puerto Real. CdC inlet is located between Ciudad del Carmen and Punta Zacatal with a minimum width of 3.9 km and an average depth of 6.4 m, the largest inlet in the lagoon system. Different authors report varying total area estimates for TL with some starting at 2500 km<sup>2</sup> [21,25], while recent studies by [26] suggest a surface area of 1930 km<sup>2</sup>, including satellite lagoons (Figure 1).

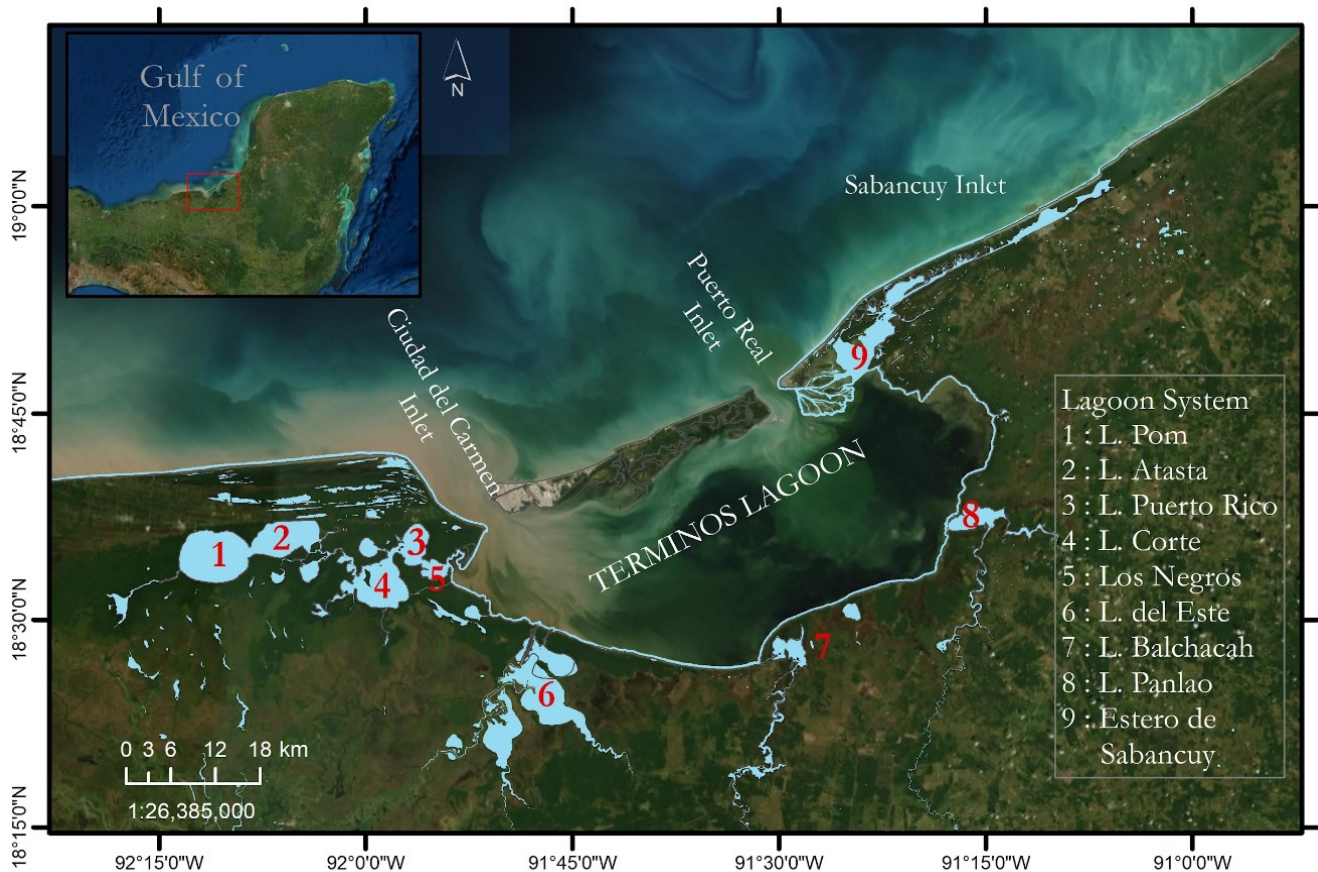


**Figure 1.** Location of the Lagoon System, Terminos Lagoon, Campeche, México.

The region has three distinct seasons: the dry season (March–May), the rainy season (June–October), and the cold fronts (also known as “Nortes”) season (November–February), the latter characterized by winter storms or strong winds caused by high-pressure systems that descend from the central plains of the United States. Some authors consider the month of May as a transition month [27]. This region is strongly influenced by mesoscale atmospheric processes, such as the trade winds, which generate a parallel circulation along the coast in a southwest direction. These winds have a seasonal pattern and are more intense from November to February with an average intensity in October, March, and April, and a significant decrease from May to September. The occurrence of “Nortes” events causes a change in local circulation from September to April, generating a storm tide inside the TL due to the accumulation of water from the GoM entering the lagoon. When these weather phenomena are not present, the wind intensity decreases, and the water volume inside the TL is restored. Generally, the wind direction of these events is from the north-northwest with a duration of 2 to 10 days [28,29]. From April to May, the diurnal cycle of the sea breeze reaches its maximum due to the trade wind’s intensity reduction. The average breeze direction alternates from southeast to northwest [7,30]. During this

period, the highest temperatures are recorded, the wind speed decreases for several hours between sea and land breeze transition, and the astronomical tide influences the circulation inside the TL [26].

During the seasons mentioned above, the hydrodynamic circulation varies due to the differences in the magnitude of forcing agents. These include river discharges, wind, circulation over the GoM continental shelf, and the astronomical tide. Refs. [31,32] describe the circulation in the Campeche Bank as characterized by an almost coast-parallel southwestward current, reversed to the northeast between September–November due to the seasonal weakening of the trade winds during summer. They also conclude that there is a semi-permanent southwestward circulation, where the preferential flow enters the TL through the PtR inlet and exits through the CdC [33]. These dynamics within the lagoon coincide with the deltas located at both inlets: one interior at PtR, mainly formed by marine material, and the other exterior at the CdC, mainly composed of river material [24]. Additionally, during “Nortes”, the internal circulation of the lagoon experiences a change in direction as a response to the external circulation forced by the winds.

## 2.2. Data

We used numerical simulations from the Weather Research and Forecasting (WRF) atmospheric model and the coastal hydrodynamical model MARS3D. The WRF simulation results were used to analyze wind patterns, assess the wind power potential, and quantify the incident solar radiation to determine the photovoltaic potential. The outputs from the MARS3D model were analyzed to characterize tidal currents and calculate their energy potential.

### 2.2.1. WRF Data

The WRF atmospheric model is a highly versatile model designed for weather forecasting and research, and has a wide range of applications, including idealized and real case simulations, air quality modeling, and ocean-atmosphere interaction studies through coupling with ocean models. WRF was developed by the National Center for Atmospheric Research (NCAR), National Oceanic and Atmospheric Administration (NOAA), National Center for Environmental Prediction (NCEP), Earth System Research Laboratory (ESRL), Air Force Weather Agency (AFWA), Naval Research Laboratory (NRL), Center for Analysis and Prediction Storms (CAPS), and the Federal Aviation Administration (FAA), and is a state of the art mesoscale numerical model aimed to enhance the understanding of atmospheric processes and improve weather prediction. The WRF database used in this work was provided by the Coastal Processes and Engineering Laboratorio from the Institute of Engineering of UNAM at Sisal, Yucatan [34]. The initial and boundary conditions for the numerical simulations were taken from the ERA-Interim atmospheric reanalysis provided by the European Center for Medium-Range Weather Forecast [35]. The numerical scheme configuration used in the simulations was based on the default of the operational forecast of the Institute of Climate Change and Atmospheric Sciences of UNAM [36], along with other standard parametrizations for tropical regions [37–39]. For more details on the WRF model, see ref. [40]. The simulation experiment consists of four nested computational domains, with data from the fourth domain used in this study. The fourth domain (D04) is centered on the southern coast of the GoM, approximately from Frontera, Tabasco, to Sabancuy, Campeche (Table 1). The WRF model variables used were  $u$  and  $v$  wind components ( $\text{ms}^{-1}$ ) at 10 m height and 1000 hPa, 10 m height wind direction ( $^{\circ}$ ), air surface temperature ( $^{\circ}\text{C}$ ), and shortwave radiation (SWDN) ( $\text{Wm}^{-2}$ ). The simulation period covered from 1 January 2015 at 00:00:00 to 31 December 2017 at 23:00:00 h, with hourly temporal resolution. The WRF outputs used to characterize wind and irradiance were validated in a previous study by [41], where the author compared measured data from a weather station in Ciudad del Carmen with the simulated time series of the same variables to ensure accuracy.

**Table 1.** Input parameters of the WRF and MARS3D model simulations.

WRF		MARS3D	
<b>Spatial resolution</b>			
93°17'32.64'' W	19°41'3.48'' N	92°12'48.24'' W	18°57'33.84'' N
90°43'55.56'' W	18°11'28.67'' N	91°13'44.04'' W	18°23'57.12'' N
Dx = 790 m	Dy = 790 m	Dx = 0.0027° (~300.3 m)	Dy = 0.0025° (~296.1 m)
<b>Vertical resolution</b>			
30 levels		20 levels	
<b>Temporal resolution</b>			
1 h		1 h	

### 2.2.2. MARS3D Data

MARS3D is a hydrodynamic model developed by the Division of Environment and Coastal Planning of IFREMER, France [42] to describe and predict the movement of fluids and related variables (temperature, salinity, etc.) for a given environment, whether it be the ocean, the continental shelf, or an estuary [43–46]. It belongs to the “3D hydrodynamic models in sigma coordinates” class, capable of simulating the transport and mixing of water masses on time scales ranging from one hour to one day. It was designed to represent the behavior of non-steady three-dimensional ocean flows, enabling the three-dimensional modeling of ocean circulation and the dispersion and transport of pollutants in the marine environment from the coastal zone to a few hundred kilometers offshore. The model is well suited for simulating sea level variations and ocean currents on a range of time scales. The MARS3D model variables used were  $u$  and  $v$  current components ( $\text{ms}^{-1}$ ) at all sigma levels to perform a velocity profile analysis (Table 1). The simulation period covered 11 months from 1 October 2019 at 00:00:00 to 30 August 2017 at 15:00:00 h, with hourly temporal resolution. The MARS3D outputs were used to characterize the currents in the area. The model validation is found in [26], where to ensure accuracy, the simulated time series were compared to measured data from a network of sensors placed along the TL.

### 2.3. Analysis

In this section, we describe the statistical analyses carried out, according to the type of energy, to evaluate the available resources and the procedure for generating the proposal for the hybrid system in the interest area. The availability and distribution of wind, irradiance, and currents were evaluated by characterizing their variability in different temporal scales. The periods of largest resource utilization were then identified. Finally, the study proposes a hybrid-renewable energy system design based on the availability and characteristics of the wind, solar and current resources in the study area. PtR and CdC were proposed as emplacement points with different characteristics according to the type of energy generation and the existing infrastructure (Figure 2). Time series for wind, solar radiation, and tidal currents were extracted from the closest grid points of the WRF and MARS3D models to the proposed emplacement points. The climatology for the entire study period and the hourly, daily, and monthly averages were obtained from these time series.

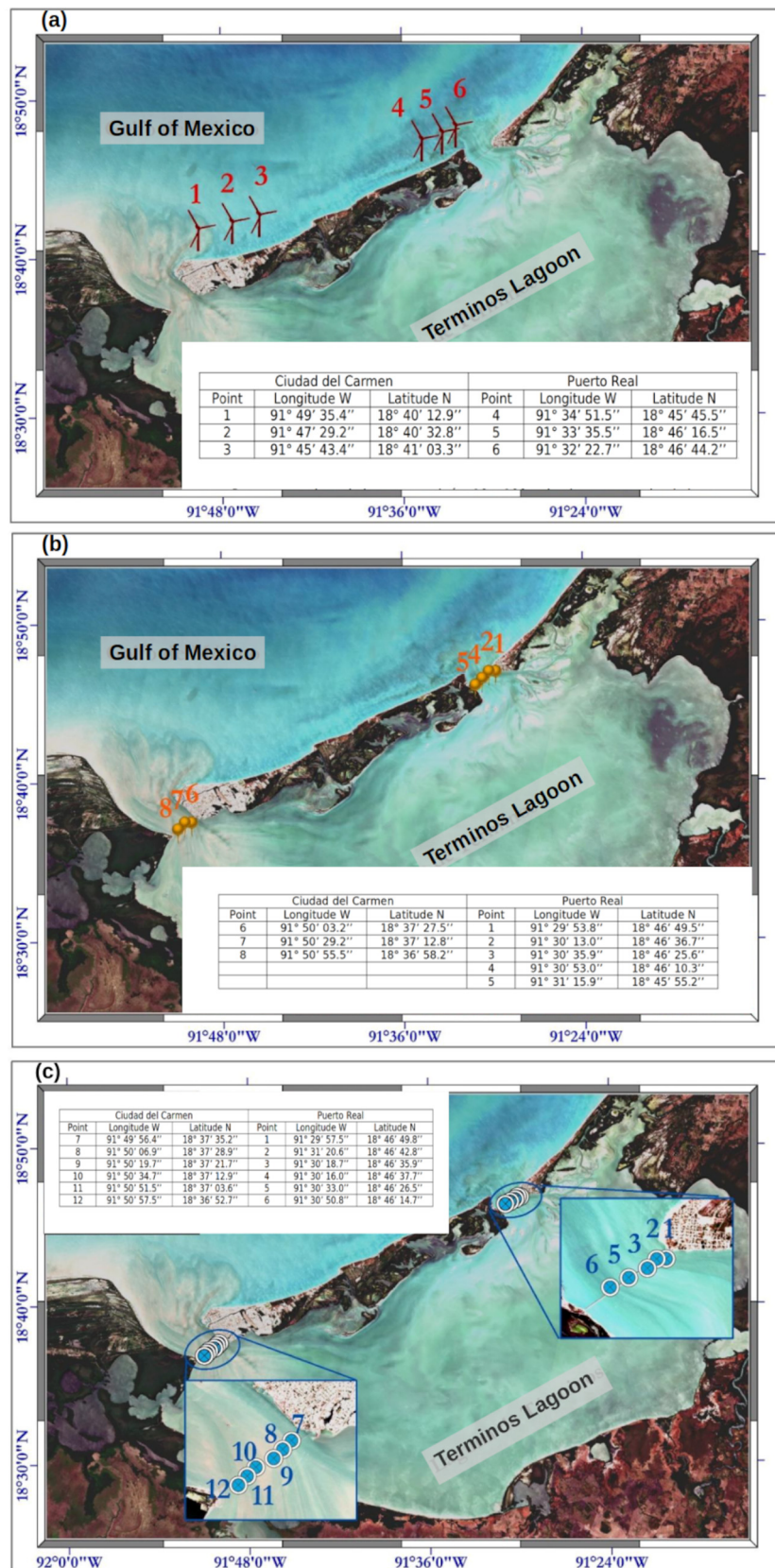


**Figure 2.** Location of the proposed emplacement points for (a) wind, (b) photovoltaic, and (c) tide. Emplacements 3 and 4 in (b,c) are not shown due to space constraints; they are located sequentially in each array.

### 2.3.1. Wind Analysis

We considered various factors to identify the optimal location for wind harnessing, including navigation and infrastructure, proximity to the coast, and the characteristics of the potential sites. Due to high-volume shipping and limited navigation at the CdC inlet and road infrastructure along the coast at the PtR inlet, we propose emplacement points for onshore–offshore wind turbines between the coastline and the 10 m isobath (Figure 2a). Such location ensures easy access to the electric grid and connection to the hybrid system. The table in Figure 2a shows the geographic coordinates of the proposed emplacement points. The wind analysis, including hourly, daily, and monthly averages, was performed at those locations, characterizing the wind speed variability at 10 m and 100 m above ground from 1 January 2015 to 31 December 2017. The data at 100 m was extrapolated from the data at the first pressure level (1000 hPa, equivalent to 111 m in height). A Weibull probability distribution analysis was performed (Equation (1)) to determine the frequency at which the highest wind speed occurs. The scale factor  $c$  determines the average wind speed, while the shape factor  $k$  characterizes the asymmetry of the distribution and provides information on the dispersion of wind speeds.

$$(V) = \frac{dF}{dV} = \frac{k}{c} \cdot \left(\frac{V}{c}\right)^{k-1} \cdot e^{-\left(\frac{V}{c}\right)^k} \quad (k > 0, V > 0, c > 1) \quad (1)$$

The cumulative frequency distribution of wind speed was obtained to determine the number of hours a given wind speed can be exceeded. Wind roses were generated to characterize the wind further and analyze its frequency, magnitude, intensity, and direction.

The maximum energy that can be extracted from the wind if all the kinetic energy is converted into useful energy, known as wind energy potential, depends on various factors such as the wind turbine, air density, rotor area, and wind speed. Wind turbines convert the wind's kinetic energy into mechanical energy by the aerodynamic rotor. These factors influence the energy transferred to the rotor, with a maximum of 59% of the available energy being extractable due to the Betz limit [47]. The wind potential of an area is sensitive to the turbine's height and the type of turbine used (IDAE, 2006 in [48]). To assess wind energy, we conducted a temporal characterization, which allows an understanding of the typical wind behavior at different periods. The Weibull probability density calculation is one method that fits the wind characteristics in most cases [6,9,48–51].

As the wind signal is amplified in the GoM region [7,50], we assessed diurnal and monthly variations in wind patterns throughout the year. The power density ( $Wm^{-2}$ ) was calculated using Equation (2) and wind data at 10 and 100 m above ground, allowing us to compare the difference in wind potential at different heights and identify the hours and months with the minimum and maximum power density. The percentage of occurrence was then determined.

$$\frac{P}{A} = \frac{1}{2} \rho V^3 \quad (2)$$

where  $V$  is the wind speed magnitude ( $ms^{-1}$ ) calculated from its meridional and zonal components, with  $V = \sqrt{(u)^2 + (v)^2}$  and its direction with  $\theta = \tan^{-1} \frac{v}{u}$ . The air density ( $\rho$  in  $kgm^{-3}$ ) was obtained based on the temperature values with Equation (3):

$$\rho = 1.225 \left( \frac{288}{t + 273} \right) e^{\left( \frac{-h}{8485} \right)} \quad (3)$$

where  $t$  is the temperature ( $^{\circ}C$ ) at 1000 hPa converted to 100 m using the standard vertical thermal gradient ( $0.65^{\circ}C/100$  m) and  $h$  the height (m).

The mean power density  $Pd$  per unit area  $A$  (Equation (4)), which provides a more accurate estimate of the wind energy potential, was calculated by incorporating the energy pattern factor  $K_e$  (as described in Equation (5)) into the analysis. The  $K_e$  factor [52] accounts for the variations in wind speed, allowing for a more reliable representation of the mean

power density. The methodology for determining the mean power density (Equation (6)) was based on research by [53,54].

$$\frac{Pd}{A} = \frac{1}{2}\rho V^3 K_e \quad (4)$$

$$K_e = \frac{1}{NV^3} \sum_{i=1}^N V_i^3 \quad (5)$$

where  $N$  is the number of hours in the evaluated period, typically one year (8760 h).  $\underline{V}$  is the mean wind speed, calculated using the equation:  $\underline{V} = \frac{1}{N} \sum_{i=1}^N V_i$  and  $V_i$  represents the instantaneous or hourly wind speed.

### 2.3.2. Irradiance Analysis

We determined five potential sites at a disused vehicle bridge over PtR, and three along the active vehicle bridge at CdC to assess the photovoltaic potential (Figure 2b). Due to the current use of the bridge at CdC, there is limited space for photovoltaic cell installation. The table in Figure 2b shows the geographic coordinates of the proposed emplacement points. To characterize the irradiance variability, we used Surface Solar Radiation (ShortWave-DowN) data since they can be considered as the Global Solar Irradiance (GSI), according to [55]. We analyzed the irradiance occurrence and temporality to assess the diurnal and monthly dynamics of the GSI pattern. From the SWDN data and the diurnal cycle results, the Peak Solar Hours (PSH) were obtained (Equation (6)). The PSH is a key parameter for evaluating global solar radiation and represents the number of hours that one square meter of horizontal surface requires to receive  $1000 \text{ Wm}^{-2}$  of irradiance in a day [56–59].

$$\text{PSH} = \frac{GSI_d}{I_i} \quad (6)$$

where  $GSI_d$  is the daily global solar irradiance ( $\text{Wm}^{-2} \text{ h}$ ), total irradiance of the diurnal cycle average and  $I_i$  the incident irradiance ( $1000 \text{ Wm}^{-2}$ ).

### 2.3.3. Tidal Currents Analysis

To assess tidal energy potential, we establish 12 emplacement points (6 at each inlet). According to [26,41], the inlets have a deeper channel at the east ( $\sim 13 \text{ m}$  in PtR and  $\sim 15 \text{ m}$  in CdC). Therefore, emplacement points closest to the deep zone were chosen in both PtR and CdC (Figure 2c), considering that generators cannot be placed in the center of the inlets due to navigation reasons. According to our literature survey [15,60,61], many submerged electrical generators have diameters ranging from 4 m to 16 m; therefore, depths greater than these should be sought. The embedded table in Figure 2c shows the geographic coordinates of the proposed emplacement points.

To analyze tidal currents variability,  $u$  and  $v$  components of the current velocity were transformed into “z” levels at each emplacement point. These data were interpolated at every 0.5 m depth, up to 10 m, to determine the magnitude and direction of the currents at each depth level. The potential energy of the currents was calculated using the interpolated velocity at different depth levels, therefore the power density was calculated using Equation (2), where the fluid density corresponds to seawater ( $\rho = 1027 \text{ kgm}^{-3}$ ). Additionally, the diurnal and monthly patterns of the tidal currents were analyzed to understand their variability throughout the year, considering their vertical variability and the appropriate depth for harnessing energy. This was achieved by calculating the hourly and monthly averages for each depth and characterizing them to determine that the optimal depth meets both technical conditions for the generators and the available power at different time scales.

An analysis of tidal amplitude was performed to determine the peak hours for tidal energy usage. The tidal amplitude, the difference between maximum and minimum levels, can vary greatly depending on location and range from a few centimeters to meters. In

this zone of the GoM, the tidal currents are significantly influenced by the vertical and horizontal movements of the water mass, which affect the speed and direction of the currents. We used the tidal predictions of the Center for Scientific Research and Higher Education of Ensenada (CICESE) to obtain the tidal amplitude for the study area. Two periods were selected for analysis: a spring tide period from 3–7 November 2009, and a neap tide period from 24–27 November 2009.

### 3. Results and Discussion

#### 3.1. Wind Assessment

The wind speed frequency distribution and the Weibull distribution analysis were performed at 10 m and 100 m heights at the CdC and PtR inlets. At 10 m height, a high probability for wind speeds between  $5 \text{ ms}^{-1}$  and  $7 \text{ ms}^{-1}$  is observed with a relative frequency of approximately 18.75%. The Weibull distribution fit shows a symmetrical curve with a maximum frequency at  $5.9 \text{ ms}^{-1}$  for CdC and  $5.8 \text{ ms}^{-1}$  for PtR; these values are classified as a medium speed for wind turbine emplacement [59]. The wind speed frequency distribution increases with height, and at 100 m height, the maximum relative frequencies are observed between  $6 \text{ ms}^{-1}$  and  $8 \text{ ms}^{-1}$ , representing 57.19% for CdC and 54.36% for PtR (Figure 3). For CdC, the maximum frequency of 20.47% is centered on  $7.28 \text{ ms}^{-1}$ , and for PtR, the maximum frequency of 19.92% occurs at  $6.43 \text{ ms}^{-1}$ . Additionally, a wind speed of  $7.6 \text{ ms}^{-1}$  for PtR has a frequency of 19.91%. These two classes account for a significant portion of the total data, up to 39.83%.

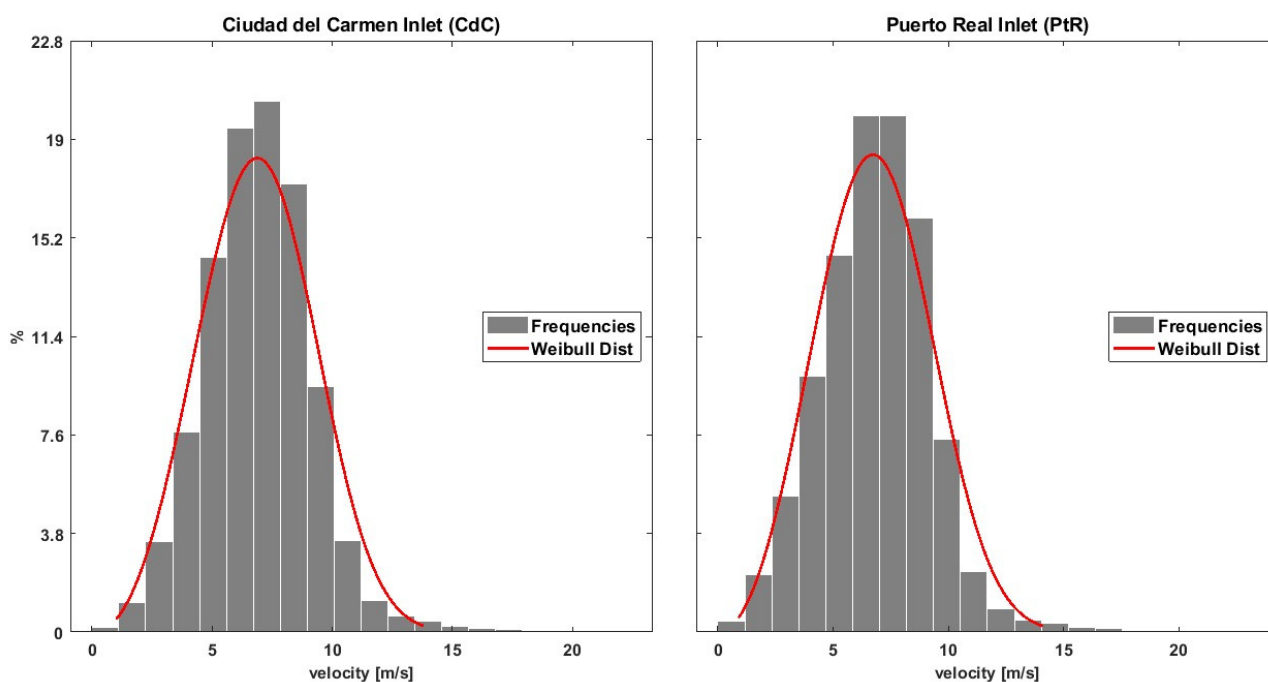


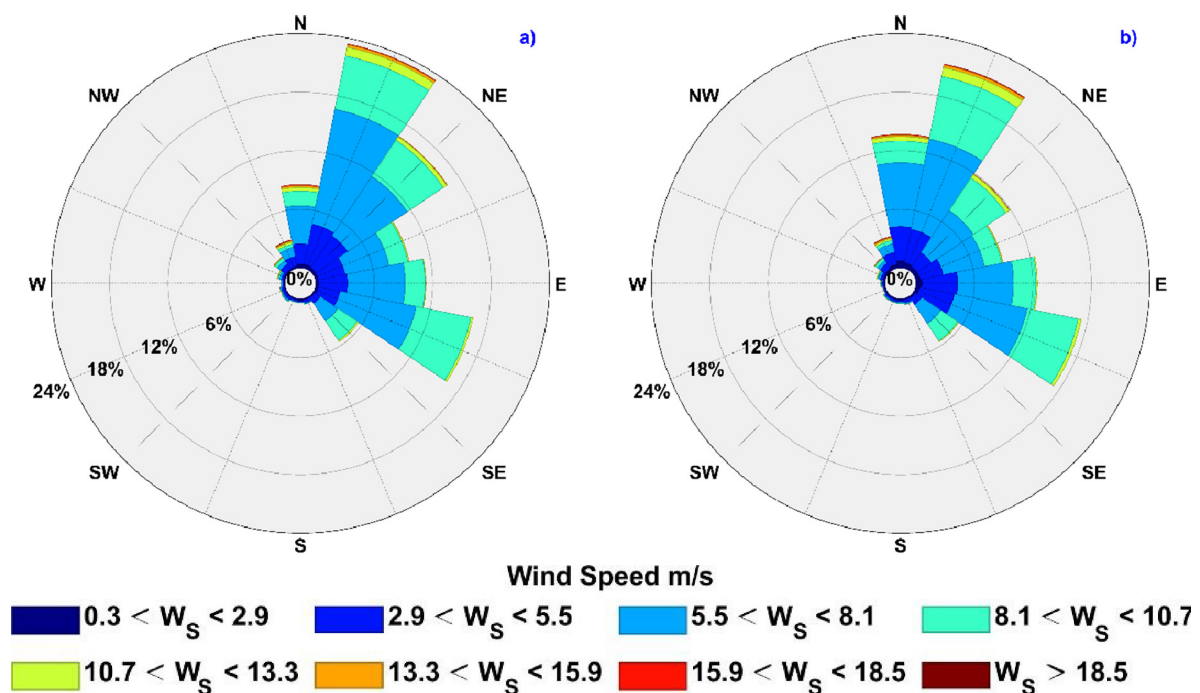
**Figure 3.** Wind speed histogram at 100 m height for CdC (right) and PtR (left) inlets, showing the corresponding Weibull distribution (red curve).

By comparing the wind speed frequency distribution at 10 and 100 m height, we observed, as expected, that wind speed increases with height. The increase in speed results from a reduced frictional drag far above the ground [6,10,50]. For our study area, this is significant, as the minimum wind speed required to consider wind turbine installation is  $5.8 \text{ ms}^{-1}$  [62]. The high wind speeds observed at both inlets of the lagoon at 100 m height make the area suitable for wind energy generation. Table 2 presents the average wind speed magnitude for the six emplacement points, with an average magnitude of  $6.94 \text{ ms}^{-1}$  obtained for the CdC inlet and  $6.85 \text{ ms}^{-1}$  for PtR.

**Table 2.** The average wind speed magnitude at each emplacement points at 100 m height.

Wind Speed ( $\text{ms}^{-1}$ )					
E1	E2	E3	Es4	E5	E6
6.97	6.93	6.91	6.85	6.86	6.85

The wind rose analysis for the six proposed emplacement points showed no significant differences in direction, frequency, and wind speed magnitude for CdC and PtR inlets. Figure 4 presents the wind roses for CdC (a) and PtR (b) considering the averaged wind speed and direction of three of the proposed emplacement points in each inlet. The wind has a predominantly north-northeast direction reaching maximum speeds in the range of  $13.3 \text{ ms}^{-1} < W_s < 15.9 \text{ ms}^{-1}$ . Both inlets exhibit a similar occurrence percentage with maximum wind speeds occurring approximately 24% of the time at CdC and 21% at PtR. The wind roses indicate two predominant wind directions, similar in both locations, as the region of TL is strongly influenced by the trade winds [26]. These two dominant directions are likely due to the influence of the trade winds blowing from the north-northeast direction and the intense effect of the breezes blowing from the east-southeast direction. These wind patterns have a seasonal variation with an increase in strength from May to September when the breeze's diurnal cycle reaches its peak intensity [7].

**Figure 4.** Rose diagrams of wind speed magnitude ( $\text{ms}^{-1}$ ), direction ( $^{\circ}$ ), and frequency (%) at (a) CdC and (b) PtR.

Considering that wind power density is one of the most critical factors in evaluating wind [9], we calculated wind power density at 10 m and 100 m above surface for the diurnal and monthly cycles. Results show an evident change in wind power density between the two heights with a maximum of  $400 \text{ Wm}^{-2}$  for the diurnal cycle at 100 m height and  $371 \text{ Wm}^{-2}$  for the monthly cycle (Figure 5b,d). On the other hand, the maximum wind power density at 10 m height was  $250 \text{ Wm}^{-2}$  for the diurnal cycle and less for the monthly cycle (Figure 5a,c). The maximum wind power density was observed at 21:00 h, and the minimum power density at 12:00 h for both the diurnal cycle at 10 m and 100 m heights (Figure 5a,b). This confirms the strong wind influence of the breeze on the area, as [7] demonstrated, finding a similar hour of the day for the maximum wind speeds. The minimum wind power density was observed in June at 10 m height and in September at

100 m height, while the maximum wind power density was observed in January at both heights (Figure 5c,d). The largest power density range was observed at 100 m in PtR with a difference of  $273 \text{ Wm}^{-2}$  between the minimum and maximum power density. A similar trend is seen in CdC with a range of  $240 \text{ Wm}^{-2}$ .

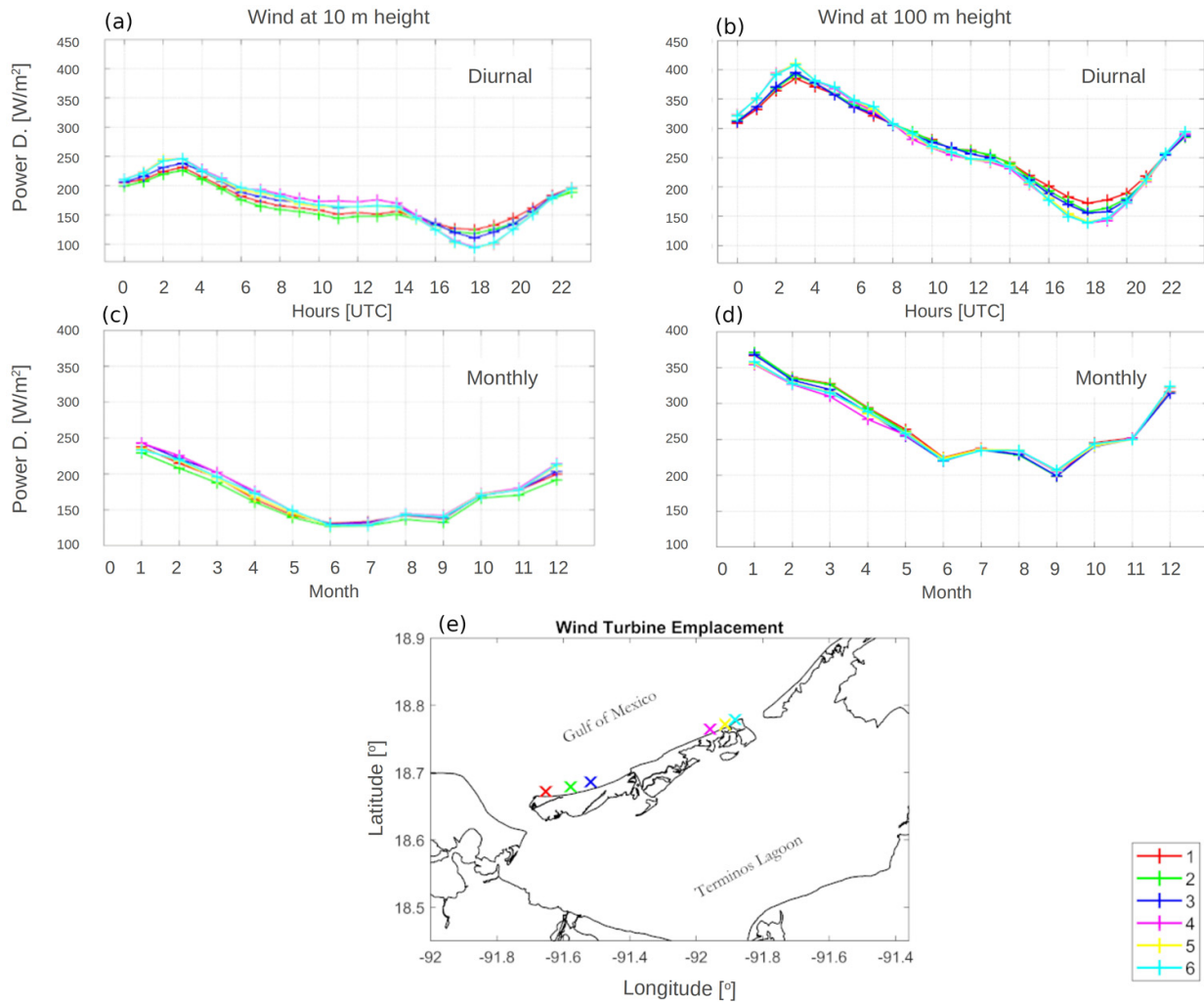


**Figure 5.** The power density variability at each emplacement points at 10 and 100 m height is shown. (a,b) show the hourly average, while (c,d) show the monthly average. (e) Indicates the location of each emplacement point (color crosses).

A mean power density of  $260.52 \text{ Wm}^{-2}$  was calculated for the six emplacement points by incorporating the  $K_e$  energy pattern factor (Equation (5)) into the mean power density equation (Equation (6)) based on the methodology of [53]. The average  $K_e$  factor for both inlets was 1.35, which is below the range between 1.45 to 4.4 proposed by [52]. Still, the Weibull  $k$  shape parameter obtained with the method of [52] is close to three for both inlets. This  $k$  value indicates the presence of constant winds in the area and a long period with winds above average, according to [9]. Additionally, [52] suggests that determining the shape parameter  $k$  and evaluating the power density yields more satisfactory results compared to other methods used in previous studies. Given the study area's average power density of  $260.52 \text{ Wm}^{-2}$ , which falls within the desirable range [53], we selected the optimal wind turbine. After considering the hub height of 100 m, we selected three wind turbine options: two three-blade and one two-blade turbine. However, it is important to note that losses due to maintenance and extreme weather events were not considered in these calculations.

We evaluated the generated power in the study area between the three wind turbine models (Aerodyn, Vestas, and Enercon, see Table 3), obtained from the 100 m height wind velocity time series from the WRF model. On average, Aerodyn and Vestas showed similar daily yield, higher than Enercon, which was approximately 1–2 MW below the other brands due to its smaller swept area. The maximum power value was 4.91 MW (Aerodyn), and the minimum was 1.16 MW (Enercon) in CdC. In PtR, the maximum power was 5.15 MW (Aerodyn), and the minimum was 1.0 MW (Enercon).

**Table 3.** Wind turbine models characteristics, the Annual Energy Produced (AEP), and the minimum and maximum Daily Energy Produced (DEP) for each inlet.

Brand	Model	Diameter (m)	Power (MW)	CdC			PtR		
				AEP (GWh)	DEP (MWh)		AEP (GWh)	DEP (MWh)	
				Total	Min	Max	Total	Min	Max
Aerodyn	SCD 8.0/168	84	8	23.29	2.04	4.91	22.94	1.75	5.15
Vestas	V164-8.0	82	8	27.15	1.94	4.68	26.72	1.67	4.91
Enercon	E-126	63.5	7.58	26.72	1.16	2.81	18.87	1.0	2.94

These results align with the findings from the power density assessment. The maximum and minimum power values in a daily cycle occurred at 21:00 and 12:00 h, respectively. In contrast, in a monthly cycle, the maximum was observed in January and the minimum in September. The Annual Energy Produced (AEP) was determined by combining the Weibull distribution of wind speeds and each wind turbine's Power Curve (PC). The Vestas wind turbine was the most productive, yielding 27.15 GWh and 26.72 GWh per year for CdC and PtR, respectively (Table 3). This highlights the significance of wind turbine characteristics in determining the usable power, as the PC considers the wind turbine's efficiency. The three-blade design of the Vestas wind turbine also offers advantages, such as better distribution of forces, higher starting torque, and improved orientation stability. Furthermore, the Load Factor (LF) or plant factor was found to be 33% on average, surpassing the average value of 25% (onshore) or 30% (offshore) reported by [63]. The results demonstrate that the Vestas wind turbine produces the most energy, achieves the best LF, and has the highest potential for energy production with an estimated average annual energy production of 26.94 GWh. However, it is important to remember that these results do not consider factors affecting the actual energy production, such as maintenance and transmission losses and other operational inefficiencies. These factors can reduce energy production by as much as 15% to 20%. It is essential to consider these losses to estimate the achievable energy production from the wind turbine accurately.

### 3.2. Irradiance Assessment

This section presents the shortwave irradiance time series (SWDN) from 1 January 2015 to 31 December 2017, including the hourly and monthly average. It also presents the analysis of the temporal distribution and occurrence of solar irradiance, the Photovoltaic Energy Generated (PEG) by a photovoltaic panel, and the Annual Energy Produced (AEP). Figure 6a shows the solar irradiance occurrence between 0 to 100  $\text{Wm}^{-2}$ , 60% of the time, with relative frequencies ranging between 2.5% to 6% in the interval between 100 to 900  $\text{Wm}^{-2}$ . The bins between 700 to 900  $\text{Wm}^{-2}$  have the highest irradiance at 6% of occurrence. The temporal variation in solar irradiance is depicted in Figure 6c, which demonstrates that the months with the highest levels of irradiance are from April to July with a peak in May and a minimum in December. This pattern aligns with the findings of [6], who reported the highest levels of solar irradiance during spring and summer, and the lowest during fall and winter.

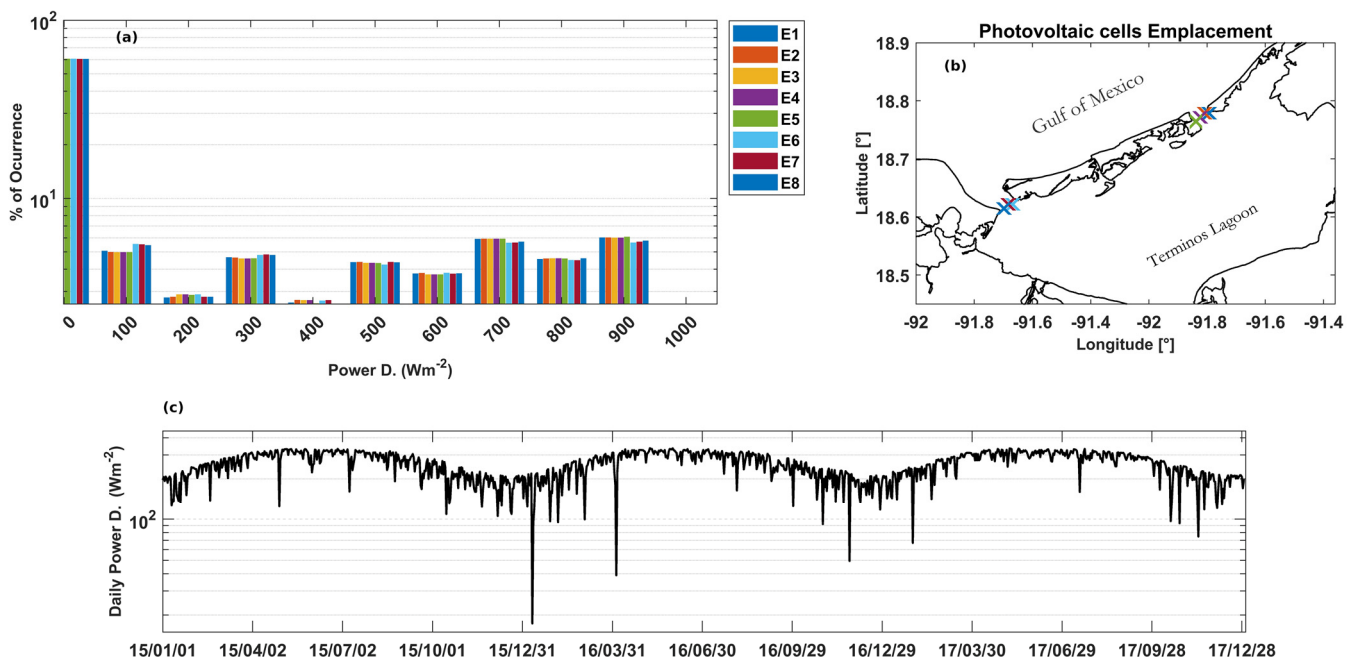


**Figure 6.** (a) Irradiance occurrence analysis, the bars represent the percentage of time that each irradiance range is observed. The colors of the bars correspond to each of the emplacement locations. (b) Shows the location of the emplacement points. (c) Shortwave radiation surface (SWDN) time series.

Figure 7a shows the diurnal cycle of solar irradiance, represented by the hourly average. It is observed that from 19:00 to 06:00 h, the solar irradiance is 0 Wm<sup>-2</sup> as it corresponds to nighttime. From 07:00 h, the solar radiation increases, reaching its peak of 895 Wm<sup>-2</sup> at 13:00 h. The solar irradiance intensity decreases to 47 Wm<sup>-2</sup> at 18:00 h and 0 Wm<sup>-2</sup> at 19:00 h, thus completing the daily cycle. Peak Solar Hours (PSH) were obtained during a diurnal cycle. For the monthly cycle in Figure 6b, December has the lowest irradiance of 184 Wm<sup>-2</sup>, and May has the highest irradiance of 311 Wm<sup>-2</sup> with a difference of 127 Wm<sup>-2</sup>. In January, the irradiance increases, reaching the maximum in May, and slightly decreases in August to 289 Wm<sup>-2</sup>, before rapidly decreasing to November with 198 Wm<sup>-2</sup> reaching the minimum in December. The difference in solar irradiance between May to August and August to December is shown in Figure 7b. During spring and summer, a difference of 22 Wm<sup>-2</sup> was obtained, while a difference of 91 Wm<sup>-2</sup> was observed in the fall and winter. The highest irradiance was observed during spring and summer and the lowest during fall and winter, which aligns with the findings of [12]. An average irradiance of 6.14 KWhm<sup>-2</sup> day<sup>-1</sup> was also obtained, which according to [12] complies with the requirement of more than 4 KWhm<sup>-2</sup> day<sup>-1</sup> for grid-connected photovoltaic installations. In addition, the authors suggest that the solar radiation levels in the coastal zone of the GoM are suitable for developing solar thermal and photovoltaic power plants. They highlight that among the states in the region, Campeche and Tamaulipas have the highest solar potential.

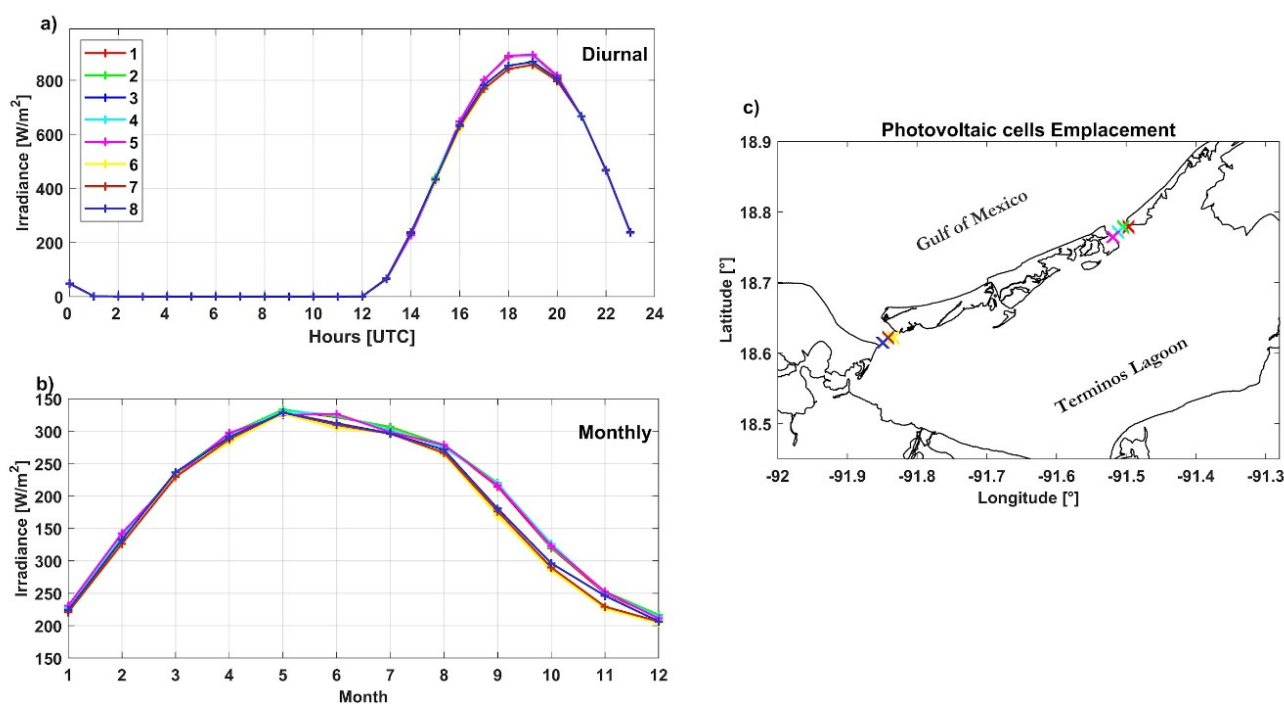


**Figure 7.** Variability of the solar irradiance: (a) hourly average irradiance, (b) monthly average, and (c) location of the emplacement sites. The colored crosses indicate the location of each emplacement point.

To determine the Generated Photovoltaic Energy (GPE), we considered a SUNPOWER Maxeon 3 photovoltaic panel with a Peak power ( $P_p$ ) of  $390 \text{ W}_p$  and obtained 6 h PSH. Table 4 summarizes the photovoltaic energy potential, including the Global Solar Irradiance (GSI), the estimated GPE, and the Annual Energy Produced (AEP) that a photovoltaic panel can generate in optimal conditions over a year.

**Table 4.** Average solar irradiance and annual energy produced for a photovoltaic panel.

GSI ( $\text{Wm}^{-2}$ )	Irradiance ( $\text{kWhm}^{-2}$ )	Photovoltaic Energy			
		$P_p$ ( $\text{W}_p$ )	PSH (h)	GPE (kWh)	AEP (kWh)
268.45	6.14	390	6	2.34	854.1

### 3.3. Currents Assessment

The results in this section present the tidal currents analysis, including the daily and monthly average, covering the period from 1 January 2009 at 00:00 h to 30 August 2010 at 15:00 h. The current energy potential is characterized by analyzing currents' velocity and predominant direction throughout the water column to determine the optimal depth for energy harvesting equipment installation. This information helps to identify the areas with the highest energy potential and optimizes the design and deployment of current energy systems. Based on the results obtained from the interpolation of current velocities at different depth levels (Figure 8), we found that the deepest areas in CdC are occupied by emplacements 7 (Figure 8g) and 8 (Figure 8h) with emplacement 7 having a maximum depth of 14.16 m, and emplacement 9 (Figure 8i) being the shallowest at 3.5 m. The deepest emplacement in PtR is situated east of the inlet, adjacent to Isla Aguada, with a 9.2 m, while the shallowest depth is observed at emplacement 5 (Figure 8e) with 4.7 m. Unlike at CdC the slope change in PtR is more gradual due to the current circulation; however, both inlets exhibit the largest depth in their eastern areas. The diurnal average vertical velocity time series at each emplacement point indicates that the highest speeds occur at the surface.

Velocities exceeding  $0.6 \text{ ms}^{-1}$  are observed at all emplacements except for emplacements 1, 6, and 7 (Figure 8a,f,g) that range between  $0.4 \text{ ms}^{-1}$  and a maximum of  $0.55 \text{ ms}^{-1}$ . The monthly variability speeds are similar at all locations and tend to decrease with increasing depth. The maximum velocities are between  $0.6$  and  $0.7 \text{ ms}^{-1}$  at a depth of  $0.5 \text{ m}$  at emplacements 2 to 5 (Figure 8b–e) and 8 to 12 (Figure 8h–l), while the minimum velocities were found near the bottom between  $0.15 \text{ ms}^{-1}$  and  $0.2 \text{ ms}^{-1}$  at emplacements 1 (Figure 8a) and 6 (Figure 8f). Emplacements in PtR (Figure 8a–f) showed larger variability along the vertical velocity profile during the diurnal cycle, while emplacements in CdC (Figure 8g–l) were the lowest. Although the speeds found in the 12 emplacements exceed  $0.5 \text{ ms}^{-1}$ , emplacements 3 to 6 (Figure 8c–f) in PtR and 9 to 12 (Figure 8h–l) in CdC have low depths, ranging between  $4.5 \text{ m}$  and  $6.5 \text{ m}$ , which may not be suitable for the standard diameter of some hydrokinetic generators. Emplacements 1 (Figure 8a) and 2 (Figure 8b) in PtR and 7 (Figure 8g) and 8 (Figure 8h) in CdC have the highest depth, however emplacements 2 and 8 have maximum speeds above  $0.6 \text{ ms}^{-1}$ , so we used them to represent each inlet for the power density calculation.

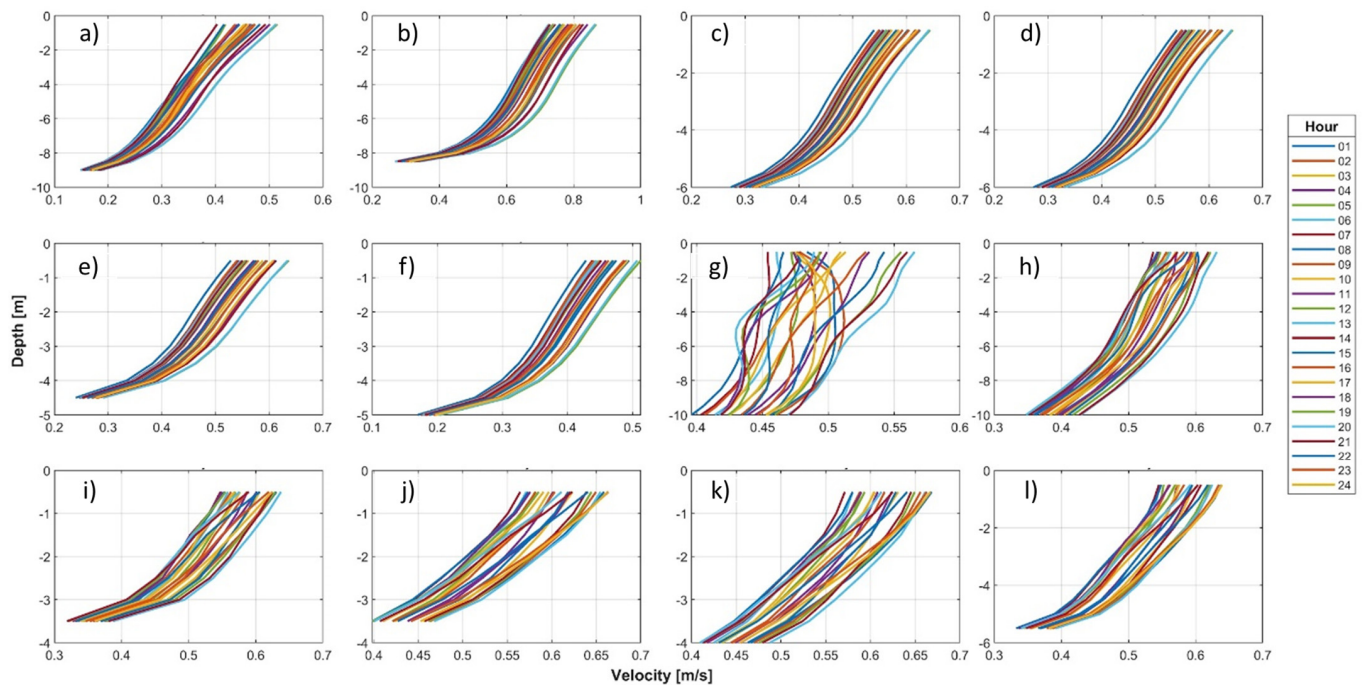


**Figure 8.** Hourly vertical profile currents average velocity with emplacement points (a–f) representing PtR and (g–l) representing CdC.

The tidal currents frequency distribution and the Weibull distribution analysis were performed at  $4 \text{ m}$  depth at the PtR and CdC inlets, as shown in Figure 9. For PtR, the maximum frequencies are observed between  $0.4 \text{ ms}^{-1}$  and  $1 \text{ ms}^{-1}$ , representing  $58.4\%$ , while for CdC the maximum frequencies are observed between  $0.2 \text{ ms}^{-1}$  and  $0.6 \text{ ms}^{-1}$ , representing  $54.3\%$ . The Weibull distribution fit shows a symmetrical curve with a maximum frequency at  $0.5 \text{ ms}^{-1}$  for PtR and  $0.4 \text{ ms}^{-1}$  for CdC.

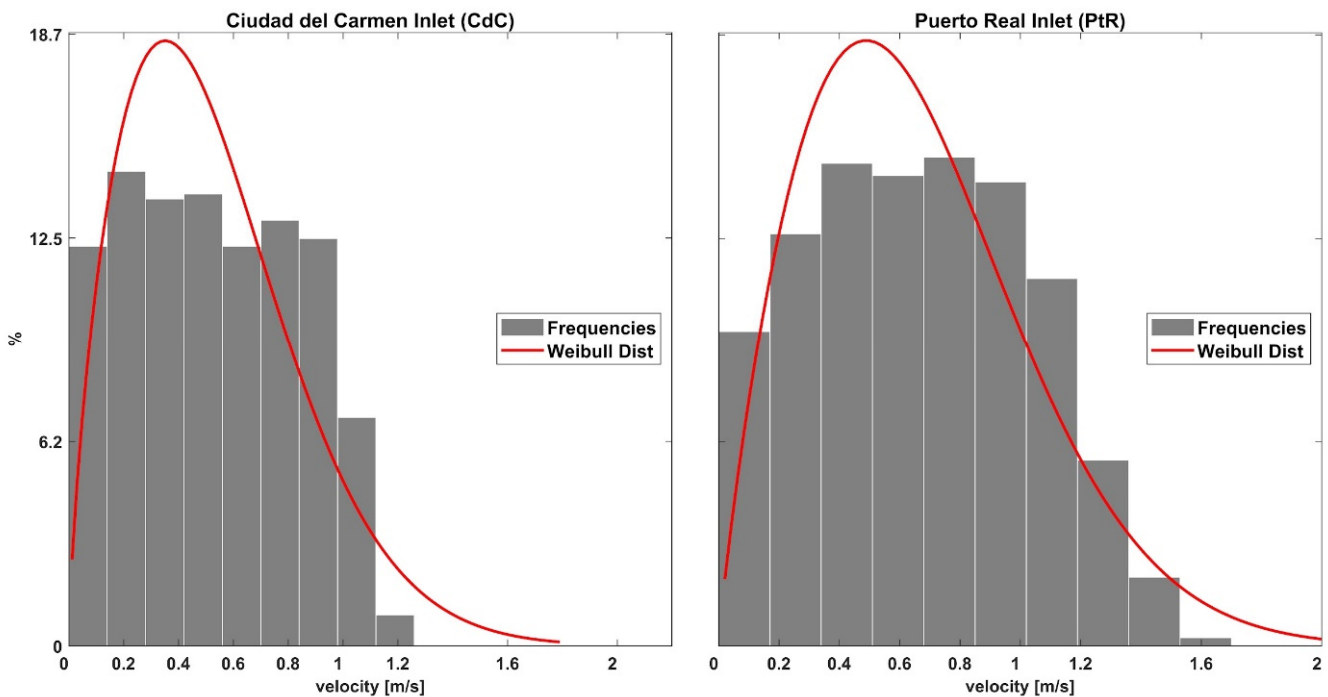


**Figure 9.** Currents speed histogram at 4 m depth for CdC (right) and PtR (left) inlets, showing the corresponding Weibull distribution (red curve).

Figure 10 presents the current direction roses at both inlets, showing two predominant directions. Figure 10a shows that the northwest direction is the most frequent, accounting for more than 50% of the total current direction which coincides with the tidal flow. The other direction, to the southeast, occurs less frequently with a presence of 30% during the ebb tide but more intense. For PtR (Figure 10b), the predominant current direction is west, with a high occurrence rate of approximately 60%. Additionally, a secondary current direction with a lesser occurrence rate of 30% is observed in the southeast direction, corresponding to the flood flow; the highest speeds are observed in both directions. These results demonstrate the strong influence of the flood flow and ebb phenomenon on the current directions [21,24,26].

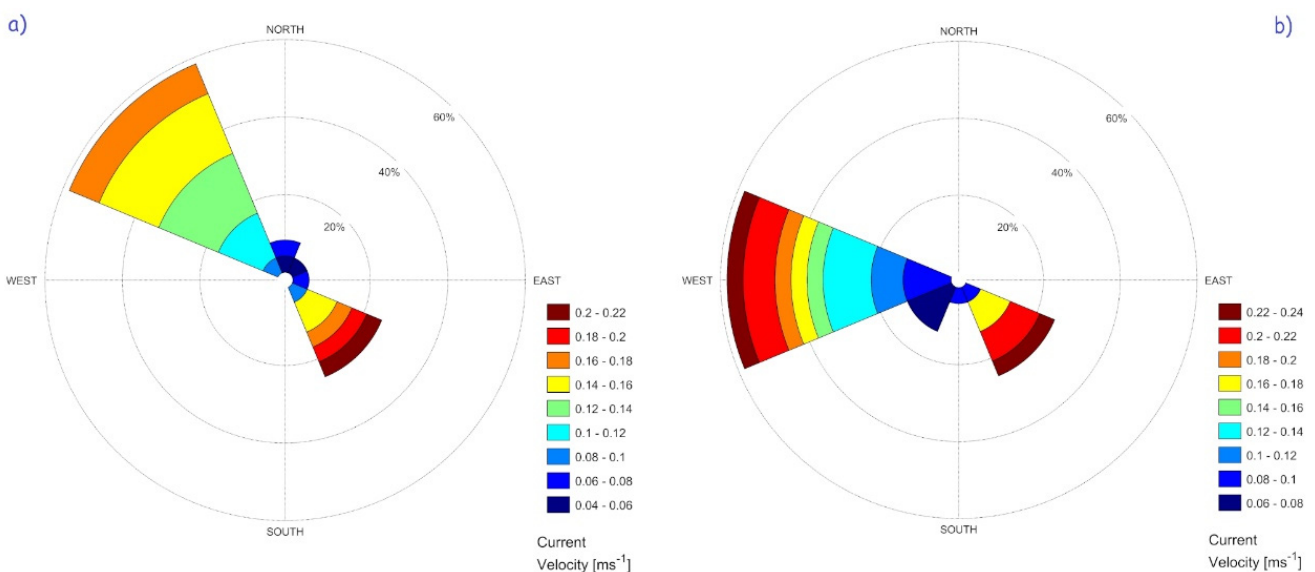


**Figure 10.** Rose diagrams of current speed magnitude ( $ms^{-1}$ ), direction ( $^{\circ}$ ), and frequency (%) at (a) CdC and (b) PtR.

The analysis of the tidal amplitude in both PtR and CdC revealed an average tidal range of 0.8 m. The predominant tide in the area is diurnal mixed on the ocean side, which becomes diurnal within the lagoon due to friction. The tidal distribution in both inlets fluctuates between  $-0.2$  m and  $0.2$  m with speeds reaching  $1.2$   $\text{ms}^{-1}$ . Despite PtR having a maximum current speed of  $1.6$   $\text{ms}^{-1}$  and CdC of  $1.2$   $\text{ms}^{-1}$ , the tidal speeds are small, ranging from  $0$  to  $0.15$   $\text{ms}^{-1}$ , and therefore, not significant [64]. The results indicate that wind is the primary driver of the circulation patterns in the TL, as reported by previous studies [64,65], and not the astronomical tides. To verify this, we computed the correlation between current speed, power density, current magnitude, tidal amplitude, and wind, using lag intervals of 6 h and 12 h. The highest correlations were found between wind and tidal amplitude with PtR showing a positive correlation of 0.9 and CdC of 0.8 with no lag for either inlet. This high correlation with wind can be attributed to the width of both inlets (approximately 3 km), which does not constrain the astronomical tidal flow, resulting in speeds of less than  $0.5$   $\text{ms}^{-1}$ .

Even though astronomical tides influence current circulation patterns in the area, rain-fall discharge and oceanic and atmospheric circulation create flows that enter the lagoon through PtR and exit through CdC. From August to September, this flow is reversed by the transit of a trapped wave to the coast [33]. The current direction aligns with the coastline, which corresponds to the channel resulting from the recirculation of currents and sediment transport. The direction change happens within a 2-to-3 h interval, suggesting that the hydrogenerator installed should be able to accommodate bidirectional flow or requires adjusting its orientation as the current direction shifts. The maximum flow velocity was observed between 01:00 and 06:00 h and between 13:00 and 18:00 h with higher speeds in PtR compared to CdC. The currents variability in both PtR (Figure 11c) and CdC (Figure 11f) show surface speeds, which range from  $0.27$   $\text{ms}^{-1}$  to  $0.86$   $\text{ms}^{-1}$  (Figure 11a) and  $0.35$   $\text{ms}^{-1}$  to  $0.63$   $\text{ms}^{-1}$  (Figure 11d), respectively. As a result, the power density in PtR ranges from 10 to  $340$   $\text{Wm}^{-2}$  (Figure 11b), whereas for CdC it ranges from 20 to  $130$   $\text{Wm}^{-2}$  (Figure 11e). The power density decreases with increasing depth, reaching values between 10 and  $40$   $\text{Wm}^{-2}$  at the maximum depth. At a depth of 4 m, a change in slope of the vertical profiles of both velocity and power density is observed with the slope decreasing and velocity and power density increasing as it approaches the surface. The results indicate that the power density of the currents is  $99.74$   $\text{Wm}^{-2}$  with an energy pattern factor  $K_e$  of 1.87 in PtR and  $114.22$   $\text{Wm}^{-2}$  with a factor  $K_e$  of 1.96 in CdC. Table 5 shows the power density according to the time of the day when the currents reach their maximum and minimum speed.

**Table 5.** Maximum and minimum current velocity (CV;  $\text{ms}^{-1}$ ) and power density (P/A;  $\text{Wm}^{-2}$ ) at 0.5 m and 4 m depth.

Period (hrs)	CdC				PtR			
	01:00–06:00		13:00–18:00		01:00–06:00		13:00–18:00	
Depth (m)	CV	P/A	CV	P/A	CV	P/A	CV	P/A
0.5	0.54–0.6	79.49–109.85	0.54–0.62	83.32–121.84	0.74–0.82	212.37–283.01	0.74–0.83	207.81–291.59
4.0	0.5–0.56	63.72–90.87	0.5–0.58	62.9–100.11	0.62–0.69	125.07–172.24	0.63–0.72	129.6–189.08

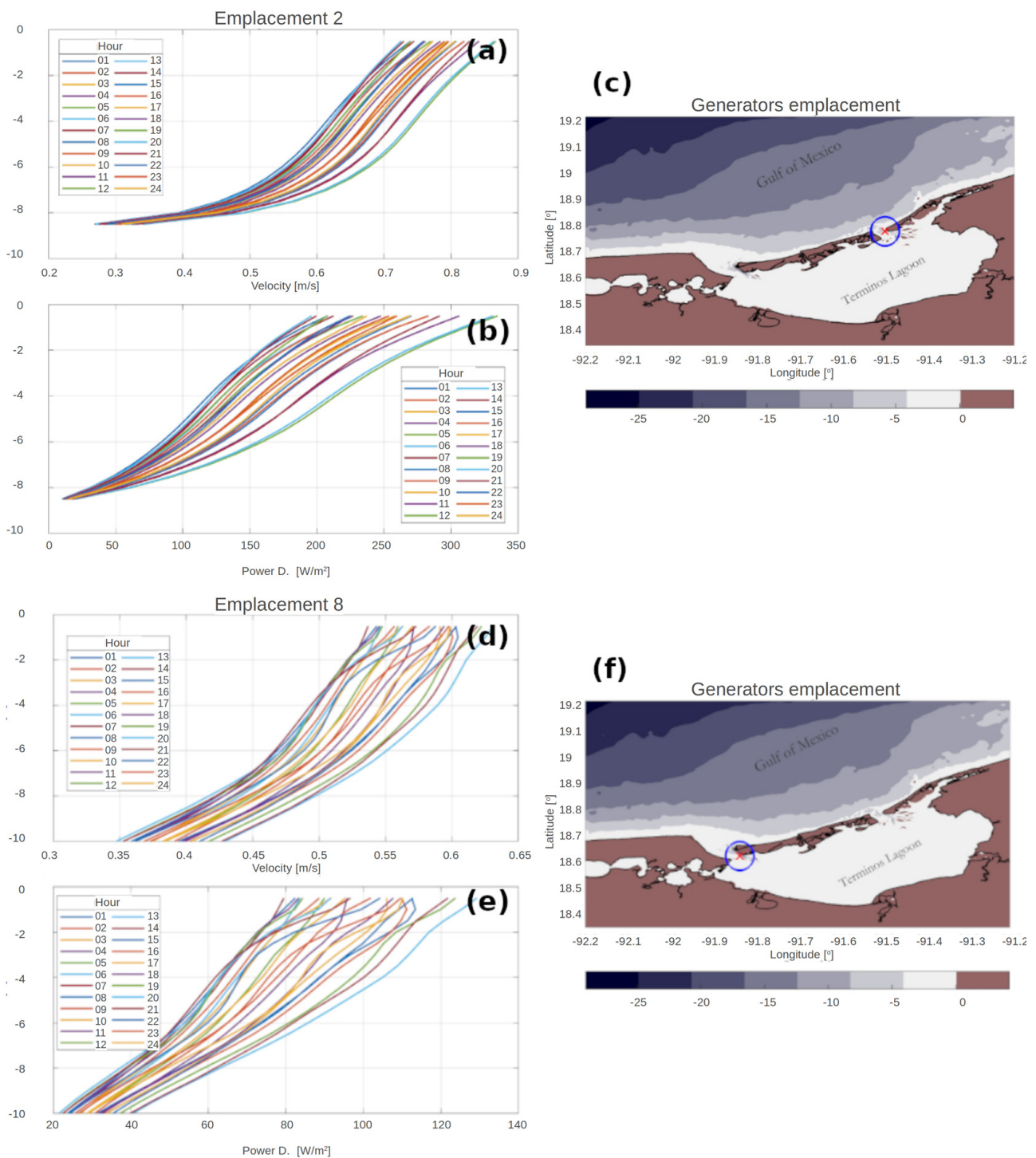


**Figure 11.** Daily average of current velocity and power density for PtR (a–c) and CdC (d–f). The vertical profile of current velocity is depicted in (a,d), while the vertical profile of power density is shown in (b,e). The geographical location of emplacement point 2 is shown in (c) and emplacement point 8 in (f). Each day’s hourly data is indicated by a different color line.

### 3.4. Hybrid System Proposal

We designed the hybrid system, including wind, photovoltaic, and tidal current harnessing (Figure 12), to integrate into the National Electric System (NES) network to supply power to the area. The next section presents a synopsis of the available resources and its components, as well as its relative importance in terms of the local grid power consumption.

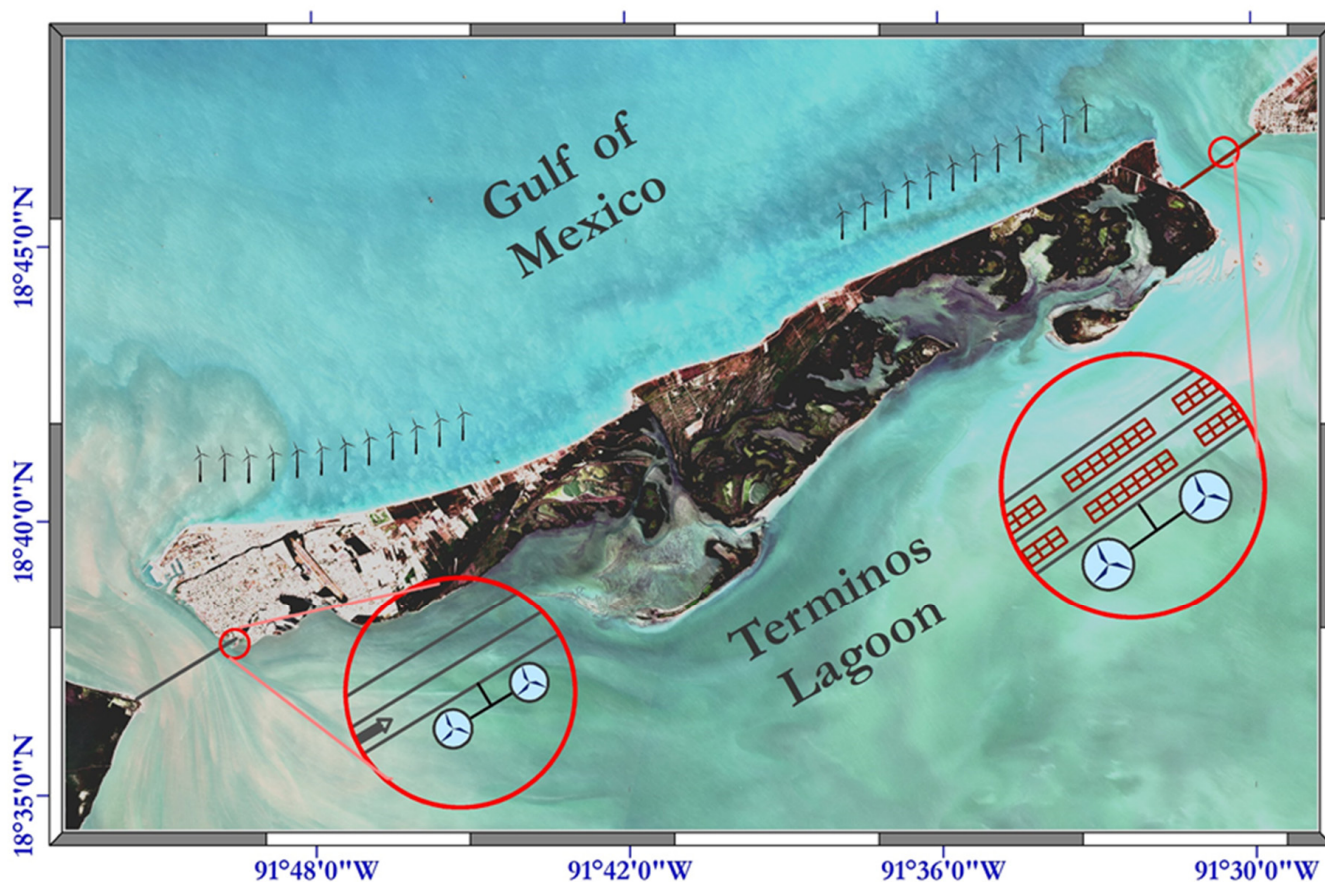


**Figure 12.** Hybrid system distribution map showing the placement of each device in its respective locations with accurate scale representation. The map also includes the relevant details and specifications of each device.

#### 3.4.1. Wind

Given the high efficiency and performance of commercial horizontal axis wind turbines (HAWT), we carried out a comparison between three different wind turbines (Table 6). As a result, we considered the Vestas V164-8.0 in the proposed system to allow for an averaged EAP of 26.94 GWh of energy and an average LF of 38.4%. On the side of CdC, large vessels, mainly from the oil sector, navigate in the area, and on the side of PtR, only smaller fishing vessels. As such, we proposed to install wind turbines along the coastal strip of Isla del Carmen. The park effect is critical in minimizing the wake effect of wind turbines on each other in a wind farm. The wake effect is the reduced wind speed downstream, resulting in a slow and turbulent flow. In a wind farm, this effect comprises the wakes from multiple turbines interacting and overlapping, leading to decreased energy production, increased turbulence, and potential damage to the turbines [6,50,66]. Wind loss and turbulence intensity are two factors associated with wind turbine placement [67]. The park effect, which involves the optimal spacing and distribution of turbines, is crucial to mitigate these impacts. Recommended minimum distances between turbines vary with turbine diameter ( $D$ ) and prevailing wind conditions, ranging from  $3D$  to  $5D$  perpendicular to the prevailing wind and  $5D$  to  $9D$  in the direction of the prevailing wind, as reported in various studies [6,50,59,66–68]. Consequently, the selected locations were between the 10 m isobath and the coastline and 1.5 km offshore, which is more than the  $9D$  value recommended for the wind park effect in the wind direction. We propose a parallel to the coastline distribution of wind turbines separated by  $4D$  perpendicular to the predominant wind direction (Figure 12 and Table 7). A total of 12 wind turbines are considered on each side of Isla del Carmen with a total of 24 wind turbines and an installed power of 192 MW. In CdC,

325.8 GWh of annual production can be obtained, and in PtR, 320.64 GWh, so the 24 wind turbines installed could achieve a generation of 646.44 GWh.

**Table 6.** Wind turbines comparison according to their efficiency and performance (HAWT). The estimated annual production (EAP) of each model for each of the mouths is also shown.

Trademark	Model	Diameter (m)	Power (MW)	EAP (GWh)	
				CdC	PtR
Aerodyn	SCD 8.0/168	84	8	23.29	22.94
Vestas	V164-8.0	82	8	27.15	26.72
Enercon	E-126	63.5	7.58	19.17	18.87

**Table 7.** Characteristics of the wind turbine arrangement for the proposed photovoltaic system.

Wind Power Plant	
Model	Vestas V164-8.0
Diameter	164 m
Rated Power	8 MW
Offshore distance	1.5 km
Max depth	10 m
Rotor height	100 m (MSL)
Diameters separation	4D
Number of emplacements	24
Installed potency	192 MW

### 3.4.2. Solar

The selection of photovoltaic panels is critical in determining the efficiency and performance of a photovoltaic system. To this end, it is important to consider factors such as the material used in the panel (monocrystalline or polycrystalline), the peak power, and efficiency of the panel. Notably, polycrystalline panels have been reported to exhibit reduced efficiency in high temperature environments when compared to monocrystalline panels [57,69,70]. The connection and number of panels used, as well as whether they are arranged in series or parallel, are also crucial. Additionally, it is imperative to evaluate the supporting components of the system, such as the inverter, controller, storage system, and monitoring system, to obtain a comprehensive photovoltaic solution. Here we selected a monocrystalline panel type from the Sun Power brand, specifically the Maxeon 3 model 390 Wp, which operates at a maximum temperature of 85 °C and has a temperature coefficient of  $-0.29\%$  per °C. The panel has a voltage ( $V_{mpp}$ ) of 64.5 V, a nominal current of 6.05 A, and an efficiency of 22.1%. The manufacturer also indicates a lifetime of 25 years with a 92% drop in production, corresponding to an annual degradation of 0.25%. The proposed photovoltaic system consists of  $7 \times 2$  panels connected in series and parallel with 4 m separation between each arrangement along and across the disused vehicular bridge at the PtR inlet (as shown in Figure 12 and Table 8). This configuration results in 394 arrangements, comprising 5516 panels with an installed power of 2.15 MW and an estimated annual production (EAP) of 4.71 GWh, assuming 6 h of solar peak. This amount of energy generation is equivalent to 1% of the energy consumption of the municipality of Carmen and 0.36% of the state of Campeche. However, accounting for the 20% system losses, the system is expected to generate energy equivalent to 0.8% of the municipality's consumption and 0.29% of the state's consumption.

**Table 8.** Characteristics of the solar panel arrangement for the proposed photovoltaic system.

Photovoltaic Power Plant	
Model	Maxeon 3
Peak power	390 Wp
Number of panels	5516
Arrangement	7 × 2
Arrangements separation	4 m
Installed potency	2.15 MW

There are various tools and platforms available to gather data on irradiance, irradiation, and the number of peak solar hours in a specific area. For example, the National Renewable Energy Laboratory's REexplorer and the Prediction of Worldwide Energy Resource (POWER) tool, can provide valuable information based on climatological analysis. The POWER platform also evaluates incident irradiance horizontally and with different inclination angles based on latitude. The Photovoltaic Geographical Information System (PVGIS) by the European Commission is another platform that provides irradiance and irradiation data [56]. Based on the information gathered from these sources and the results obtained in this study, the recommended orientation of the photovoltaic panels is to the south with an inclination angle equal to the area's latitude. This configuration minimizes the shadow effect between panels and allows space for power lines and maintenance personnel circulation. For the system, it is suggested to use INGECON Sun Power Series UB (1800 kW/1500 V) inverters, an INGECON Plant Controller, and a monitoring system.

### 3.4.3. Currents

For the study area, we propose a design with a turbine rotor diameter between 3–6 m integrated according to the depth of the area. Characteristic turbine speeds, such as the starting speed, nominal speed, and cut-off speed, are suitable for the site's velocities (less than  $1 \text{ ms}^{-1}$ ), and the nominal power is adjusted accordingly. The turbine would have to be adapted to 6 m in diameter, and a depth of 4 m is necessary to install the rotor hub or shaft, which is permissible according to the site's depth. To increase flow intensity in areas with low speeds, a casing using the Venturi effect is proposed. OpenCentre turbines with a diameter of 3–4 m, rotor depth, and optimized operating speeds are recommended in shallow sites with small vessel navigation. However, this proposal is only for significant emplacements 1 and 2 in PtR and 7 and 8 in CdC using SeaGen turbines. Up to 32 turbines are proposed, 16 in each inlet. For installation, it is suggested that two turbines are mounted on a single arm and in turn to the bridge pile, which will contain the mechanism to lower it to the depth of the site and raise it for maintenance. The turbines will have a separation of 8 m on the single arm, measured between the extremes of the diameter of each turbine. The separation between groups of turbines would be 40 m with one pile containing a turbine and the next without a turbine (Figure 12 and Table 9). We propose using submerged horizontal axis turbines with the apex of the blades located at least 1 m below sea level and 1 m away from the bottom. Since these turbines' PCs are still unavailable, we assumed that the average efficiency of hydrokinetic turbines is 30%. Based on the current velocity analysis and the proposed turbine placement, an EAP of 237.16 MWh for PtR and 271.59 MWh for CdC can be obtained through tidal currents.

**Table 9.** Characteristics of the current turbine arrangement for the proposed photovoltaic system.

Tidal Currents Power Plant	
Diameter	6 m
Rotor depth	4 m
Turbine arrangement	2 on each pile
Separation between turbines	8 m
Separation between arrays	40 m
Power density in CdC	114.22 Wm <sup>-2</sup>
Power density in PtR	99.74 Wm <sup>-2</sup>
Total turbines	32

#### 3.4.4. Hybrid Configuration

We estimate an AEP of 651.66 GWh, of which wind would contribute 646.44 GWh, solar radiation 4.71 GWh, and tidal currents 0.509 GWh. However, these values are not definitive, as they need to account for each system's efficiency, cavitation, or thrust coefficient in the case of currents. These values will be lower under a more precise assessment considering efficiencies and losses; therefore, production will decrease. Assuming a 20% decrease due to efficiencies and various losses, an annual energy of 521.33 GWh is feasible, which is still enough produced energy. In the state of Campeche, during 2018, there was an energy consumption of 1315.61 GWh and of 472.9 GWh in the Carmen Municipality. Table 10 shows the energy contribution the hybrid system could contribute to the energy supply. The location of the hybrid system is viable since the potential generation of 521.33 GWh represents 39.61% of the state's consumption or 10.21% higher than the consumption of the Carmen municipality.

**Table 10.** Annual Energy Produced (AEP) by the hybrid system and its contribution from each of the evaluated systems, concerning the energy consumption of the Carmen municipality and the state of Campeche for the year 2018.

System	AEP GWh			
	AEP GWh	AEP GWh −20% (Losses)	Relationship by Consumption in:	
			Carmen Municipality (%)	Campeche State (%)
Wind	646.44	517.15	>9.36	39.30
Photovoltaic	4.71	3.77	0.8	0.29
Tidal currents	0.509	0.407	0.086	0.03
<b>Hybrid</b>	<b>651.66</b>	<b>521.33</b>	<b>&gt;10.25</b>	<b>39.62</b>

The hybrid power system increases reliability due to the complementary nature of the power generation systems from renewable sources, reducing the variability between their sources [4,9,14,71,72]. This proposal highlights the significance of implementing a hybrid system, as the three evaluated systems complement each other, consistent with the findings of [14,72]. The wind system generates more energy at night when demand is higher. In contrast, the photovoltaic system generates more electricity during the day when wind speeds are lower due to breezes. The proposed hybrid system would be connected to the grid, largely avoiding the generation of electricity with fossil fuels and reusing existing infrastructure. Furthermore, it minimizes the impact on fauna. To resolve the intermittency caused by the absence of radiation or wind, a storage system could be added to the hybrid system in order to allow for a constant supply of generated energy. In addition, the proposed inverters and controllers are compatible with an energy storage system, which could be incorporated into the plant. Although, out of the scope of this study, it should be mentioned that hybrid systems can be optimized using specialized software, which can yield the optimal configuration of the system [73].

#### 4. Conclusions

This work proposes a hybrid power system for the Terminos Lagoon region, combining wind, solar, and tidal energy sources. The proposed system would allow for substituting a significant part of the energy demand with renewables, preventing GHG emissions during the project's lifetime. Additionally, hybrid systems improve reliability. Our analysis of numerical simulations using the WRF and MARS3D models has identified a high potential for wind and solar energy, while tidal currents' contribution may be too small to be viable. In any case, tidal energy requires further research and development.

Our study evaluated the area's wind, photovoltaic, and tidal current resources. We found that the Vestas wind turbine was the most suitable for the hybrid system with an estimated AEP of 517.15 GWh. The photovoltaic potential of the area was moderate with a power density of  $268.45 \text{ Wm}^{-2}$  for six peak solar hours, but implementation on the CdC bridge may be costly. The tidal current potential was limited due to shallow depths and low velocities, and further technical analysis is required to implement this component. Overall, the wind and photovoltaic components of the proposed system have the highest energy contribution, while the current section requires further research.

Our results indicate that the proposed hybrid system has significant energy potential in wind and irradiance. Although the contribution of currents is not considerable (0.509 GWh), the influence of the tide is predictable and has a dynamic effect throughout the day in the ebb or flow direction. Furthermore, our findings have important implications for the region's energy needs. In 2018, the municipality of Carmen consumed 472.9 GWh out of the total energy consumption of 1315.61 GWh in the state of Campeche. Our proposed hybrid system, located in a viable location, could generate 521.33 GWh, representing 39.63% of the state's consumption or 10.24% greater than the consumption of the municipality of Carmen. Various analyses, such as economic, environmental impact, technical justification, life cycle, and greenhouse gas mitigation analyses are necessary to assess the project's viability, including a more detailed study of the hybrid system components and options (such as energy storage). However, our study provides a promising foundation for developing a renewable energy system that could significantly reduce the region's dependence on non-renewable energy sources.

**Author Contributions:** Conceptualization, C.S.-R.y.H., C.M.A. and M.E.A.-A.; methodology, C.M.A., M.E.A.-A., B.F.-E. and C.S.-R.y.H.; formal analysis, C.S.-R.y.H., M.E.A.-A., B.F.-E., E.G.-C. and A.C.-R.E.; validation, C.S.-R.y.H.; resources, M.E.A.-A. and C.M.A.; investigation, C.S.-R.y.H., M.E.A.-A., B.F.-E., E.G.-C. and A.C.-R.E.; Writing—original draft, C.S.-R.y.H., C.M.A. and M.E.A.-A.; Writing—review & editing, C.M.A., M.E.A.-A., B.F.-E. and E.G.-C. All authors have read and agreed to the published version of the manuscript.

**Funding:** This work was partly funded by CONACYT FORDECYT-PRONACES grant 21088 (Ciencia de Frontera).

**Data Availability Statement:** The data presented in this study will be made available on figshare.com upon acceptance of the manuscript, and the link will be provided in this section.

**Acknowledgments:** The authors acknowledge Gonzalo Uriel Martín Ruiz, Camilo Rendón Valdez, Juan Alberto Gómez Liera and José López González for their technical assistance. B.F.E acknowledges support from CONACYT FORDECYT-PRONACES project 21088 (Ciencia de Frontera). This work benefited from ChatGPT, which provided helpful style suggestions and feedback on the writing of this paper.

**Conflicts of Interest:** The authors declare no conflict of interest. The funders had no role in the design of the study; in the collection, analyses, or interpretation of data; in the writing of the manuscript; or in the decision to publish the results.

## References

1. IPCC. *IPCC, 2014: Climate Change 2014: Mitigation of Climate Change. Contribution of Working Group III to the Fifth Assessment Report of the Intergovernmental Panel on Climate Change*; IPCC: Rome, Italy, 2014.
2. Fajardo-Díaz, J.L.; García-González, J.M.; García-Saldívar, V.M. Evaluación Del Potencial Eólico de Una Zona Del Estado de Zacatecas, México. *Tecnol. Ciencia, Educ.* **2010**, *25*, 95–98.
3. Instituto para la Diversificación y Ahorro de la Energía (IDAE). *Resumen Del Plan de Energías Renovables 2011–2020*; Instituto para la Diversificación y Ahorro de la Energía: Madrid, Spain, 2011.
4. Fernández Ribaya, Y. Sistema Híbrido (Solar-Eólico) Con Apoyo de Gas Natural Para La Generación de Energía Eléctrica En Baja California Sur (México). Ph.D. Thesis, Master Universitario en Ingeniería Energética, Universidad de Oviedo, Oviedo, Spain, 2012.
5. REN21. *Renewables 2020 Global Status Report*; REN21: Paris, France, 2020.
6. Hernandez-Escobedo, Q.; Rodríguez-García, E.; Saldaña-Flores, R.; Fernández-García, A.; Manzano-Agugliaro, F. Solar Energy Resource Assessment in Mexican States along the Gulf of Mexico. *Renew. Sustain. Energy Rev.* **2015**, *43*, 216–238. [[CrossRef](#)]
7. Gille, S.T.; Llewellyn Smith, S.G.; Statom, N.M. Global Observations of the Land Breeze. *Geophys. Res. Lett.* **2005**, *32*, 1–4. [[CrossRef](#)]
8. Allende-Arandía, M.E.; Zavala-Hidalgo, J.; Romero-Centeno, R.; Franklin, G.L.; Taylor-Espinosa, N.; Osorio-Tai, M.E. Large Diurnal Wind Variability over the Western and Northern Campeche Bank Caused by the Low Latitude of the Yucatan Peninsula and Its Interaction with Easterlies. *Atmos. Res.* **2022**, *265*, 105888. [[CrossRef](#)]
9. Perea-Moreno, A.-J.; Alcalá, G.; Hernandez-Escobedo, Q. Seasonal Wind Energy Characterization in the Gulf of Mexico. *Energies* **2019**, *13*, 93. [[CrossRef](#)]
10. Carrasco-Díaz, M.; Rivas, D.; Orozco-Contreras, M.; Sánchez-Montante, O. An Assessment of Wind Power Potential along the Coast of Tamaulipas, Northeastern Mexico. *Renew. Energy* **2015**, *78*, 295–305. [[CrossRef](#)]
11. Riveros-Rosas, D.; Herrera-Vázquez, J.; Pérez-Rábago, C.A.; Arancibia-Bulnes, C.A.; Vázquez-Montiel, S.; Sánchez-González, M.; Granados-Agustín, F.; Jaramillo, O.A.; Estrada, C.A. Optical Design of a High Radiative Flux Solar Furnace for Mexico. *Sol. Energy* **2010**, *84*, 792–800. [[CrossRef](#)]
12. Villicaña-Ortiz, E.; Gutiérrez-Trashorras, A.J.; Paredes-Sánchez, J.P.; Xiberta-Bernat, J. Solar Energy Potential in the Coastal Zone of the Gulf of Mexico. *Renew. Energy* **2015**, *81*, 534–542. [[CrossRef](#)]
13. Mundo-Hernández, J.; de Celis Alonso, B.; Hernández-Álvarez, J.; de Celis-Carrillo, B. An Overview of Solar Photovoltaic Energy in Mexico and Germany. *Renew. Sustain. Energy Rev.* **2014**, *31*, 639–649. [[CrossRef](#)]
14. Vega-Sánchez, M.A.; Castañeda-Jiménez, P.D.; Peña-Gallardo, R.; Ruiz-Alonso, A.; Morales-Saldaña, J.A.; Palacios-Hernández, E.R. Evaluation of Complementarity of Wind and Solar Energy Resources over Mexico Using an Image Processing Approach. In Proceedings of the 2017 IEEE International Autumn Meeting on Power, Electronics and Computing (ROPEC), Ixtapa, Mexico, 8–10 November 2017; pp. 1–5.
15. Alcérrecá-Huerta, J.C.; Encarnacion, J.I.; Ordoñez-Sánchez, S.; Callejas-Jiménez, M.; Gallegos Diez Barroso, G.; Allmark, M.; Mariño-Tapia, I.; Silva Casarín, R.; O’Doherty, T.; Johnstone, C. Energy Yield Assessment from Ocean Currents in the Insular Shelf of Cozumel Island. *J. Mar. Sci. Eng.* **2019**, *7*, 147. [[CrossRef](#)]
16. Mejía-Olivares, C.J.; Haigh, I.D.; Wells, N.C.; Coles, D.S.; Lewis, M.J.; Neill, S.P. Tidal-Stream Energy Resource Characterization for the Gulf of California, México. *Energy* **2018**, *156*, 481–491. [[CrossRef](#)]
17. Molina Pérez, E. Estimación Analítica y Evaluación Económica Del Potencial Energético de Las Corrientes Marinas En El Canal de Infiernillo, Golfo de California. Ph.D. Thesis, Universidad Nacional Autónoma de México, Mexico City, Mexico, 2016.
18. Polo, J.M.; Rodríguez, J.; Sarmiento, A. Potencial de Generación de Energía a Lo Largo de La Costa Colombiana Mediante El Uso de Corrientes Inducidas Por Mareas. *Rev. Ing.* **2008**, *28*, 99–105. [[CrossRef](#)]
19. Kavadias, K.A.; Triantafyllou, P. Hybrid Renewable Energy Systems’ Optimisation. A Review and Extended Comparison of the Most-Used Software Tools. *Energies* **2021**, *14*, 8268. [[CrossRef](#)]
20. Come Zebra, E.I.; van der Windt, H.J.; Nhumaio, G.; Faaij, A.P.C. A Review of Hybrid Renewable Energy Systems in Mini-Grids for off-Grid Electrification in Developing Countries. *Renew. Sustain. Energy Rev.* **2021**, *144*, 1–23. [[CrossRef](#)]
21. David, L.T.; Kjerfve, B. Tides and Currents in a Two-Inlet Coastal Lagoon: Laguna de Términos, Mexico. *Cont. Shelf Res.* **1998**, *18*, 1057–1079. [[CrossRef](#)]
22. Instituto Nacional de Ecología (Mexico), Mexico; Secretaría de Medio Ambiente, Recursos Naturales; Pesca. *Programa de Manejo Del Area de Protección de Flora y Fauna “Laguna de Términos”, México*; Instituto Nacional de Ecología: Mexico City, Mexico, 1997; p. 166.
23. Gutiérrez-Estrada, M.; Castro del Río, A. Origen y Desarrollo Geológico de La Laguna de Términos. In *Ecología de los Sistemas Costeros en el Sureste del Golfo de México: La Región de la Laguna de Términos*; UNAM-OEA: Mexico City, Mexico, 1988; pp. 89–110.
24. Amado Yáñez, C. *Batimetría, Salinidad, Temperatura y Distribución de los Sedimentos Recientes de la Laguna de Términos, Campeche, México*; Instituto de Geología: Mexico City, Mexico, 1963.
25. Robadue, D.; Calderon, R.; Oczkowski, A.; Bach, L.; Cepeda, M.F. *Characterization of the Region of the Laguna de Términos Campeche*; The Nature Conservancy, University of Rhode Island: Kingston, RI, USA, 2004. Available online: [https://www.crc.uri.edu/download/23s\\_L1Profile\\_Draft\\_Terminos\\_2004.pdf](https://www.crc.uri.edu/download/23s_L1Profile_Draft_Terminos_2004.pdf) (accessed on 28 April 2023).

26. Contreras Ruiz Esparza, A.; Douillet, P.; Zavala-Hidalgo, J. Tidal Dynamics of the Terminos Lagoon, Mexico: Observations and 3D Numerical Modelling. *Ocean Dyn.* **2014**, *64*, 1349–1371. [[CrossRef](#)]
27. Guerra-Santos, J.J.; Kahl, J.D.W. Redefining the Seasons in the Términos Lagoon Region of Southeastern México: May Is a Transition Month, not a Dry Month. *J. Coast. Res.* **2018**, *34*, 193–201. [[CrossRef](#)]
28. Romero-Centeno, R.; Zavala-Hidalgo, J.; Gallegos, A.; O'Brien, J.J. Isthmus of Tehuantepec Wind Climatology and ENSO Signal. *J. Clim.* **2003**, *16*, 2628–2639. [[CrossRef](#)]
29. Yáñez-Arancibia, A.; Day Jr, J.W. Ecological Characterization of Terminos Lagoon, a Tropical Lagoon-Estuarine System in the Southern Gulf of Mexico. *Oceanol. Acta* **1982**, *5*, 431–440.
30. Taylor-Espinosa, N. Análisis y Visualización de La Componente Diurna de Los Vientos En El Sur Del Golfo de México. Ph.D. Thesis, Universidad Nacional Autónoma De México, Mexico City, Mexico, 2009.
31. Dubranna, J.; Pérez-Brunius, P.; López, M.; Candela, J. Circulation over the Continental Shelf of the Western and Southwestern Gulf of Mexico. *J. Geophys. Res. Ocean.* **2011**, *116*, 1–17. [[CrossRef](#)]
32. Zavala-Hidalgo, J.; Morey, S.L.; O'Brien, J.J. Seasonal Circulation on the Western Shelf of the Gulf of Mexico Using a High-resolution Numerical Model. *J. Geophys. Res. Ocean.* **2003**, *108*, 1–19. [[CrossRef](#)]
33. Zavala-Hidalgo, J.; Romero-Centeno, R.; Mateos-Jasso, A.; Morey, S.L.; Martínez-López, B. The Response of the Gulf of Mexico to Wind and Heat Flux Forcing: What Has Been Learned in Recent Years? *Atmósfera* **2014**, *27*, 317–334. [[CrossRef](#)]
34. LIPC UNAM Observatorio Costero Del Sureste. Available online: <http://ocse.mx/en/experimento/torre-sisal> (accessed on 28 April 2023).
35. Dee, D.P.; Uppala, S.M.; Simmons, A.J.; Berrisford, P.; Poli, P.; Kobayashi, S.; Andrae, U.; Balmaseda, M.A.; Balsamo, G.; Bauer, P.; et al. The ERA-Interim Reanalysis: Configuration and Performance of the Data Assimilation System. *Q. J. R. Meteorol. Soc.* **2011**, *137*, 553–597. [[CrossRef](#)]
36. Ocean-Atmosphere Interaction Group Meteorology Forecast WRF V. 2017. Available online: <http://grupo-iao.atmosfera.unam.mx/pronosticos/index.php/meteorologia> (accessed on 28 April 2023).
37. Tewari, M.; Chen, F.; Wang, W.; Dudhia, J.; LeMone, M.A.; Mitchell, K.; Ek, M.; Gayno, G.; Wegiel, J.; Cuenca, R.H. Implementation and Verification of the Unified NOAA Land Surface Model in the WRF Model (Formerly Paper Number 17.5). In Proceedings of the 20th Conference on Weather Analysis and Forecasting/16th Conference on Numerical Weather Prediction, Seattle, WA, USA, 10–12 January 2004; pp. 11–15.
38. Gunwani, P.; Mohan, M. Sensitivity of WRF Model Estimates to Various PBL Parameterizations in Different Climatic Zones over India. *Atmos. Res.* **2017**, *194*, 43–65. [[CrossRef](#)]
39. Fonseca, R.; Zorzano-Mier, M.; Azua-Bustos, A.; González-Silva, C.; Martín-Torres, J. A Surface Temperature and Moisture Intercomparison Study of the Weather Research and Forecasting Model, In-situ Measurements and Satellite Observations over the Atacama Desert. *Q. J. R. Meteorol. Soc.* **2019**, *145*, 2202–2220. [[CrossRef](#)]
40. Skamarock, W.; Klemp, J.B.; Dudhia, J.; Gill, D.O.; Barker, D.M.; Duda, M.G.; Huang, X.Y.; Wang, W.; Powers, J.G. A Description of the Advanced Research WRF Version 3. NCAR/TN-475+STR NCAR. *Tech. Rep.* **2008**, *113*. [[CrossRef](#)]
41. Gómez de la Peña, E. Estudio Numérico de La Circulación y Aireación Asociadas Al Grijalva-Usumacinta En Laguna de Términos, Campeche. Ph.D. Thesis, Universidad Nacional Autónoma de México, Mexico City, Mexico, 2019.
42. Lazure, P.; Jégou, A.-M. 3D Modelling of Seasonal Evolution of Loire and Gironde Plumes on Biscay Bay Continental Shelf. *Oceanol. Acta* **1998**, *21*, 165–177. [[CrossRef](#)]
43. Lazure, P.; Dumas, F. An External-Internal Mode Coupling for a 3D Hydrodynamical Model for Applications at Regional Scale (MARS). *Adv. Water Resour.* **2008**, *31*, 233–250. [[CrossRef](#)]
44. Lazure, P.; Garnier, V.; Dumas, F.; Herry, C.; Chifflet, M. Development of a Hydrodynamic Model of the Bay of Biscay. *Valid. Hydrol. Cont. Shelf Res.* **2009**, *29*, 985–997. [[CrossRef](#)]
45. Douillet, P. Tidal Dynamics of the South-West Lagoon of New Caledonia: Observations and 2D Numerical Modelling. *Oceanol. Acta* **1998**, *21*, 69–79. [[CrossRef](#)]
46. Douillet, P.; Ouillon, S.; Cordier, E. A Numerical Model for Fine Suspended Sediment Transport in the Southwest Lagoon of New Caledonia. *Coral Reefs* **2001**, *20*, 361–372. [[CrossRef](#)]
47. Omar, G.-S. *Energías Renovables Una Perspectiva Ingenieril*; Trillas: Mexico City, Mexico, 2004.
48. Almonacid, A.; Nahuelhual, L. Estimación Del Potencial Eólico y Costos de Producción de Energía Eólica En La Costa de Valdivia, Sur de Chile. *Agro Sur* **2009**, *37*, 103–109. [[CrossRef](#)]
49. Carta, J.A.; Ramirez, P.; Velazquez, S. A Review of Wind Speed Probability Distributions Used in Wind Energy Analysis: Case Studies in the Canary Islands. *Renew. Sustain. Energy Rev.* **2009**, *13*, 933–955. [[CrossRef](#)]
50. Omar, G.-S. *Energía Eólica Para Generación Eléctrica*; Trillas: Mexico City, Mexico, 2015.
51. Rodríguez-Hernandez, O.; Martinez, M.; Lopez-Villalobos, C.; Garcia, H.; Campos-Amezcu, R. Techno-Economic Feasibility Study of Small Wind Turbines in the Valley of Mexico Metropolitan Area. *Energies* **2019**, *12*, 890. [[CrossRef](#)]
52. Akdağ, S.A.; Dinler, A. A New Method to Estimate Weibull Parameters for Wind Energy Applications. *Energy Convers. Manag.* **2009**, *50*, 1761–1766. [[CrossRef](#)]
53. Manwell, J.F.; McGowan, J.G.; Rogers, A.L. *Wind Energy Explained: Theory, Design and Application*; John Wiley & Sons: Chichester, UK, 2009; ISBN 0470686286.

54. Dogara, M.D.; Aboh, H.O.; Gyuk, P.M.; Onwumere, M.K.O. The Use of Energy Pattern Factor (EPF) in Estimating Wind Power Density. *Sci. World J.* **2016**, *11*, 27–30.
55. Lara-Fanego, V.; Ruiz-Arias, J.A.; Pozo-Vázquez, D.; Santos-Alamillos, F.J.; Tovar-Pescador, J. Evaluation of the WRF Model Solar Irradiance Forecasts in Andalusia (Southern Spain). *Sol. Energy* **2012**, *86*, 2200–2217. [[CrossRef](#)]
56. Pareja Aparicio, M. *Energía Solar Fotovoltaica: Cálculo de Una Instalación Aislada*; Marcombo: Barcelona, Spain, 2009; ISBN 8426715265.
57. Morán, F.A.; Facchini, M.L.; Pontoriero, D.H.; Doña, V.M. Inserción de Generación Distribuida a Través de Instalaciones Fotovoltaicas Domiciliarias Ajustadas a Las Curvas Típicas de Demanda Residencial. *Av. Energías Renov. Medio Ambient.* **2009**, *13*, 93–99.
58. Ramos López, H.; Luna Puente, R. Diseño de Un Sistema Fotovoltaico Integrado a La Red Para El Área de Estacionamiento de La Universidad Tecnológica de Salamanca. Master's Thesis, Centro de Investigación en Materiales Avanzados S.C., Chihuahua, Mexico, 2014.
59. Vega de Kuyper, J.C.; Ramírez Morales, S. *Fuentes de Energía, Renovables y no Renovables—Aplicaciones*; Alfaomega: Bogotá, Colombia, 2020; ISBN 9786077078210.
60. Ramón Grünwald, A. Estudio de La Generación Energética Con Turbinas Hidráulicas En Las Corrientes Marinas. Ph.D. Thesis, Universidad Politécnica de Cartagena, Cartagena, Spain, 2012.
61. Norris, J.; Bryden, I. European Marine Energy Centre: Facilities and Resources. *Proc. Inst. Civ. Eng.* **2007**, *160*, 51–58. [[CrossRef](#)]
62. Villarrubia, M. *Energía Eólica*; Ceac: Barcelona, Spain, 2004.
63. Hughes, G. The Performance of Wind Farms in the United Kingdom and Denmark. *Renew. Energy Found.* **2012**, *48*, 46.
64. Graham, D.S. Circulation of Two Multipass Estuaries in the Gulf of Mexico. *Coast. Eng. Proc.* **1982**, *1*, 2595–2609.
65. Kjerfve, B. Comparative oceanography of coastal lagoons. In *Estuarine Variability*; Elsevier: Amsterdam, The Netherlands, 1986; pp. 63–81.
66. Sun, H.; Gao, X.; Yang, H. A Review of Full-Scale Wind-Field Measurements of the Wind-Turbine Wake Effect and a Measurement of the Wake-Interaction Effect. *Renew. Sustain. Energy Rev.* **2020**, *132*, 110042. [[CrossRef](#)]
67. Chamorro, L.P.; Porte-Agel, F. Turbulent Flow inside and above a Wind Farm: A Wind-Tunnel Study. *Energies* **2011**, *4*, 1916–1936. [[CrossRef](#)]
68. González-Longatt, F.; Wall, P.; Terzija, V. Wake Effect in Wind Farm Performance: Steady-State and Dynamic Behavior. *Renew. Energy* **2012**, *39*, 329–338. [[CrossRef](#)]
69. Torres-Pacheco, S.; Jurado-Pérez, F.; Granados-Lieberman, D.; Lozano-Luna, A. Eficiencia En Paneles Solares. *Rev. Diseño Innov.* **2018**, *2*, 9–21.
70. Raúl Germán Cordero. Sunfields Europe. Available online: <https://www.sfe-solar.com/paneles-solares/tipos/> (accessed on 28 April 2023).
71. Miglietta, M.M.; Huld, T.; Monforti-Ferrario, F. Local Complementarity of Wind and Solar Energy Resources over Europe: An Assessment Study from a Meteorological Perspective. *J. Appl. Meteorol. Climatol.* **2017**, *56*, 217–234. [[CrossRef](#)]
72. Jurasz, J.; Piasecki, A.; Wdowikowski, M. Assessing Temporal Complementarity of Solar, Wind and Hydrokinetic Energy. In Proceedings of the E3S Web of Conferences, Krakow, Poland, 17–19 May 2016; EDP Sciences: Les Ulis, France, 2016; Volume 10, p. 00032.
73. Kefif, N.; Melzi, B.; Hashemian, M.; Assad, M.E.H.; Hoseinzadeh, S. Feasibility and Optimal Operation of Micro Energy Hybrid System (Hydro/Wind) in the Rural Valley Region. *Int. J. Low-Carbon Technol.* **2022**, *17*, 58–68. [[CrossRef](#)]

**Disclaimer/Publisher's Note:** The statements, opinions and data contained in all publications are solely those of the individual author(s) and contributor(s) and not of MDPI and/or the editor(s). MDPI and/or the editor(s) disclaim responsibility for any injury to people or property resulting from any ideas, methods, instructions or products referred to in the content.